PHASE FIELD FRACTURE MODELING OF FATIGUE CRACK GROWTH AND DUCTILE DAMAGE

A THESIS SUBMITTED TO
THE GRADUATE SCHOOL OF NATURAL AND APPLIED SCIENCES
OF
MIDDLE EAST TECHNICAL UNIVERSITY

BY

SARIM WASEEM

IN PARTIAL FULFILLMENT OF THE REQUIREMENTS
FOR
THE DEGREE OF MASTER OF SCIENCE
IN
AEROSPACE ENGINEERING

JULY 2023

Approval of the thesis:

PHASE FIELD FRACTURE MODELING OF FATIGUE CRACK GROWTH AND DUCTILE DAMAGE

submitted by **SARIM WASEEM** in partial fulfillment of the requirements for the degree of **Master of Science in Aerospace Engineering Department, Middle East Technical University** by,

Prof. Dr. Halil Kalıpçılar
Dean, Graduate School of **Natural and Applied Sciences** _____

Prof. Dr. Serkan Özgen
Head of Department, **Aerospace Engineering** _____

Assoc. Prof. Dr. Tuncay Yalçınkaya
Supervisor, **Aerospace Engineering, METU** _____

Examining Committee Members:

Prof. Dr. Demirkan Çöker
Aerospace Engineering, METU _____

Assoc. Prof. Dr. Tuncay Yalçınkaya
Aerospace Engineering, METU _____

Assoc. Prof. Dr. Cihan Tekoğlu
Mechanical Engineering, TOBB ETÜ _____

Assoc. Prof. Dr. Hüsnü Dal
Mechanical Engineering, METU _____

Assist. Prof. Dr. Görkem Eğemen Güloğlu
Aerospace Engineering, METU _____

Date:21.07.2023

I hereby declare that all information in this document has been obtained and presented in accordance with academic rules and ethical conduct. I also declare that, as required by these rules and conduct, I have fully cited and referenced all material and results that are not original to this work.

Name, Surname: Sarim Waseem

Signature :

ABSTRACT

PHASE FIELD FRACTURE MODELING OF FATIGUE CRACK GROWTH AND DUCTILE DAMAGE

Waseem, Sarim
M.S., Department of Aerospace Engineering
Supervisor: Assoc. Prof. Dr. Tuncay Yalçınkaya

July 2023, 86 pages

The modeling of fracture is a computationally challenging task due to the inherent discontinuities involved. The characteristic features of the phase field methodology circumvent these limitations through a diffuse interface approach to crack growth. In this thesis, the phase field approach to brittle fracture is expanded to cover both fatigue and ductile fracture based on the existing methodologies described in the literature, with some novel features added to simulate more complex behavior.

Two fatigue models are simulated with additional features in both designed to capture the crack growth retardation phenomenon, which has previously not been studied in a phase field framework. For one, the fatigue damage accumulation algorithm is altered to include a damage threshold. This is done to simulate crack closure effects and by extension, crack growth retardation effects due to overload. For the second model, a temporal fatigue damage accumulation system based on a representative load is simulated, additionally incorporating a zone based crack retardation mechanism that responds to single cycle overloads. These features allow both models to more realistically simulate complex variable amplitude loading cases restricted to the tensile region. The fatigue models are found capable of simulating crack growth re-

tardation in the wake of applied overloads, with varying levels of success in matching experimental results.

A third phase field model is used to simulate failure due to plastic deformation. A classical phenomenological uncoupled damage model is incorporated into a phase field ductile failure framework to allow it to accurately capture plastic damage evolution in complex stress states as well as allow more precise calibration. A damage threshold is applied to control the evolution of damage around the critical failure strain. The model is able to reproduce experimental load-displacement responses, plastic deformation and crack patterns for the given parameter set for various benchmark specimens.

Keywords: Phase Field, Fatigue, Plasticity, Fracture, Overload, Crack retardation, Crack propagation

ÖZ

YORULMA ÇATLAK BÜYÜMESİ VE SÜNEK HASARIN FAZ ALAN KIRILMA METODU İLE MODELLENMESİ

Waseem, Sarim
Yüksek Lisans, Havacılık ve Uzay Mühendisliği Bölümü
Tez Yöneticisi: Doç. Dr. Tuncay Yalçınkaya

Temmuz 2023 , 86 sayfa

Çatlak modellenmesi, doğasında bulunan süreksizlikler nedeniyle hesaplama açısından zorlu bir görevdir. Faz alanı yönteminin karakteristik özellikleri, çatlak büyümesine yönelik bir yayılma arayüzü yaklaşımıyla bu sınırlamaların üstesinden gelir. Bu tezde, gevrek kırılma için faz alanı yaklaşımı, literatürde açıklanan mevcut yöntemlere dayanarak yorulma ve sünek kırılma konularını kapsayacak şekilde genişletilmiş ve daha karmaşık davranışları simüle etmek için bazı yeni özellikler eklenmiştir.

İki yorulma modeli, çatlak büyümesi geciktirme fenomenini yakalamak için tasarlanmış ek özelliklerle simüle edilmiş ve bu daha önce faz alanı çerçevesinde incelenmemiştir. Birinci model için, yorulma hasar birikimi algoritması bir hasar eşiği içerecek şekilde değiştirilmiştir. Bu, çatlak kapanma etkilerini ve dolayısıyla aşırı yük nedeniyle çatlak büyümesini geciktirme etkilerini simüle etmek için yapılmıştır. İkinci model için, temsili bir yük temeline dayalı zamansal yorulma hasar birikimi sistemi simüle edilmiş ve tek çevrim aşırı yüklemelere yanıt olarak hareket eden bir bölge tabanlı çatlak geciktirme mekanizması da eklenmiştir. Bu özellikler, her iki modelin de gerçekçi bir şekilde gerilim bölgesine sınırlı karmaşık değişkenli yükleme durum-

larını simüle etmesine olanak sağlar. Yorulma modellerinin, uygulanan aşırı yüklemelerin ardından çatlak büyümesini geciktirme yeteneğine sahip olduğu ve deneysel sonuçlarla farklı düzeylerde başarı oranlarına sahip olduğu bulunmuştur.

Plastik deformasyona bağlı kırılmayı simüle etmek için üçüncü bir faz alanı modeli kullanılır. Klasik fenomenolojik ayrışmamış hasar modeli, bir faz alanı sünek kırılma çerçevesine dahil edilerek, karmaşık gerilim durumlarında plastik hasar gelişimini doğru bir şekilde yakalamasına ve daha hassas kalibrasyon yapmasına olanak tanır. Hasar eşiği, kritik hasar gerilimi etrafındaki hasarın evrimini kontrol etmek için uygulanır. Model, çeşitli referans örnekler için verilen parametre setine göre deneysel yük-deplasman tepkimelerini başarılı bir şekilde yeniden üretebilir.

Anahtar Kelimeler: Faz Alanı, Yorgunluk, Plastisite, Kırılma, Çatlak geciktirme, Çatlak yayılımı

For my mother, whose effort I parade as talent

ACKNOWLEDGMENTS

I would like to start by expressing my deepest gratitude to my supervisor, Assoc. Prof. Dr. Tuncay Yalçınkaya for his guidance and support and for finding faith in me when I could not.

I would like to thank Can Erdoğan for his invaluable collaboration, without whom the standard of this thesis would be far lower. And the rest of the solid mechanics group for their inputs and company.

İlbilge Umay Aydıner, without whom I'd be nowhere. Yağmur Göçmen for her confidence, support and consistent knowledge of where the roof is.

Omar Daoud for his invaluable companionship, who found me fallen over and got me back on my feet time after time, with style and grace. And Elif E. Kaptan prior to whom I have no idea how either of us were getting on with life.

M. Yousuf Mahmood, who is one of the best men I know and whose ideas of me I am constantly trying to live up to.

My grandparents, whose love keeps me on Earth. My sisters Yamna and Nawal, who constantly outperform and inspire me. My parents for their enduring support and love.

There are countless names to thank here that go unmentioned. I have always had the good fortune of exquisite company and I am grateful for all of it.

TABLE OF CONTENTS

LIST OF TABLES

TABLES

LIST OF FIGURES

FIGURES

CHAPTER 1

INTRODUCTION

A relatively recent computational approach to simulating crack growth is the phase field method, which is a diffuse interface methodology developed as a computationally advantageous solution scheme for sharp interface problems. It functions through the introduction of an additional degree of freedom, namely the phase field parameter, which at different values represents different material phases and facilitates a smooth transition between them, thereby eliminating discontinuous sharp interfaces and their associated computational problems. In the context of crack growth, the two phases that are represented are undamaged material and fully fractured material. Through this method, various forms of mechanical failure may be simulated.

Fatigue is one of the most common and dangerous forms of mechanical failure. Under the influence of a fluctuating load, fatigue failure can occur at stress states that are well below even a metal's elastic limit let alone its ultimate tensile strength. Therefore, designs that are sufficiently safe against ductile failure may be vulnerable against fatigue to the point of catastrophic failure. This makes the prediction of fatigue failure in materials and structures a pivotal cornerstone of engineering design. Due to the economic connotations, it is not simply enough to be over-conservative with our estimations of fatigue life, therefore accuracy in predicting fatigue life and fatigue crack paths is pivotal to balance both safety and financial considerations efficiently.

While fatigue remains the dominant failure mechanism in practical applications, metal forming and other production processes that involve heavy plastic deformation are primarily concerned with the evolution of ductile damage under various stress states. Being able to predict the evolution of damage during plastic deformation is vital in the production of reliable mechanical components.

Both damage mechanisms have been explored heavily through experimental data, and several computational models have been developed based on this data for both fatigue and ductile failure. However, modeling of fracture through the finite element method (FEM) has several inherent complications involved in the description of a discrete crack surface namely due to the involved discontinuities. Methodologies have been developed to circumvent these issues in modeling crack growth, for example, the extended finite element method (XFEM) [1], which avoids a need for remeshing through a local enrichment of the shape functions that solves the discontinuities involved. The cohesive zone model [2] is another well established methodology, describing the cohesive forces involved when crack surface separation occurs at a predefined region.

The phase field methodology provides an excellent alternative to these computational methods for modeling crack growth. In this thesis, the applicability and versatility of the phase field method is studied in the context of both fatigue and ductile crack initiation and subsequent propagation.

This chapter introduces the core ideas around which this thesis is based and is organized as thus: The following section provides a brief introduction to the development of the phase field method for brittle failure. The next section covers the development of formulations for fatigue fracture and its modeling through the phase field method. Following this, the crack retardation phenomenon is discussed, focusing on its nature and the methods developed to model it. The subsequent section covers the modeling of ductile fracture and the advantages of doing so through the phase field methodology, while the final section provides an outline for the thesis.

1.1 Phase Field Approach to Fracture

The phase field paradigm was originally developed for dual phase evolution problems through the introduction of an additional degree of freedom. The two phases are described through the phase field parameter, with a smooth transition between them that eliminates the computational complexities of an evolving discrete boundary. In the context of fracture, the two states are described as intact material and completely fractured material, with a length scale parameter determining the size of the transition

zone between them.

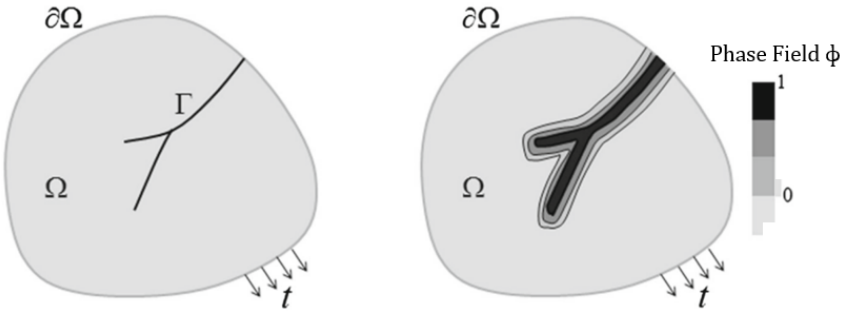

Figure 1.1: Discrete crack (left) vs. phase field crack (right) [3]

The adaptation of the phase field method to fracture is based on the variational approach to Griffith's theory of crack propagation (see [4]), developed by Francifort and Marigo (see [5]) which poses the evolution of cracks as an energy minimization problem. The heart of phase field fracture is the description of the crack surface over the domain in terms of an auxiliary variable, termed the phase field parameter. This was done by Bourdin (see [6]), who defines the crack surface based on Ambrosio and Tortorelli's regularized minimization of a Mumford Shah type functional (see [7], [8]), smoothening out jump discontinuities, with convergence to the realistic crack surface acting as a limit case as the length scale parameter tends towards 0. Originally developed to describe discrete segments in images, the framework has been adapted to describe the distribution of cracks over the domain, with the length scale acting as a regularizing parameter. Later, Miehe et al. [9] formalized the approach, as well as introduced some pivotal computational aspects that facilitated the FEM implementation of the phase field brittle fracture paradigm.

With sharp discontinuities eliminated, the phase field method is able to track crack growth without the need for any further ad-hoc criteria to determine crack paths as well as no requirement for element separation, deletion or remeshing. Furthermore, it is capable of capturing more complex behavior like crack branching.

While it boasts great computational advantages, the phase field method naturally has its drawbacks with their own computational costs. One of these being that a refined mesh is required along the crack path. Solutions to this problem have involved the

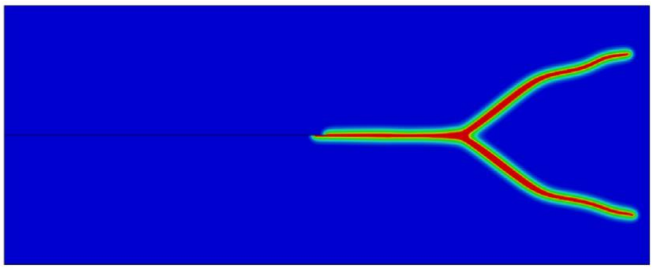

Figure 1.2: Phase field crack branching [10]

introduction of adaptive re-meshing strategies (see [11, 12]). More efficient solution schemes such as Quasi-Newton schemes [13] and line search methods [14] have also been utilized.

Quasi-static brittle fracture behavior only applies to specific materials, necessitating more advanced models to describe more complex material behavior. Using the brittle crack growth framework as the foundation, the model has been extended to other modes of material failure such as dynamic fracture [15], fracture in materials with anisotropic fracture toughness [16], corrosion fracture [17], polcrystaline fracture [18] among several others.

The extension of the framework to both the fatigue and ductile environments is discussed in the following sections.

1.2 Fatigue Crack Growth

The first studies of the fatigue fracture phenomenon were done by Wöhler [19] to explain the failure of railway axles, finding that fatigue failures can occur at stress levels well below the load levels associated with static failures. His experiments led to the development of S-N curves, which highlight the inverse relationship between the amplitudes of applied fluctuating stresses and the number of applied loading cycles it took for complete fracture. The micro-mechanical mechanisms of fatigue in metals were later studied, confirming that even at lower stress levels, micro-cracks

developed in plastic slip bands. This is due to inevitable stress concentrations causing plastic localization in the poly-crystalline structure, with slip irreversibility leading to the micro-cracks eventually growing and evolving into macro-cracks under consistently fluctuating loading conditions [20]. Miner's rule [21] introduced the concept of cumulative damage in fatigue, introducing an additive rule to predict the crack life in cases where loads of varying amplitudes were applied.

To describe the stress intensity at the crack tip, Irwin [22] introduced the stress intensity factor concept, which is one of the most dominant methodologies employed in linear elastic fracture. To avoid the numerical pitfalls of infinite stress singularities at crack tips, the stress intensity factor at crack tips is described instead,

$$K = f(a/w)\sigma\sqrt{\pi a} \tag{1.1}$$

where $f(a/w)$ is a geometric constant, dependent on the structure being studied and a is the crack length. σ is the applied stress. This concept was instrumental in the development of analytical laws to define the crack growth rate.

Fatigue crack life has been described through three distinct phases. These are crack initiation, stable crack growth and unstable crack growth respectively. The fundamental approach to fatigue fracture may be best represented by the prolific Paris and Erdogarn law [23], linking the growth rate of a crack exposed to a fluctuating load, to the difference in stress intensity factors at the maximum and minimum load conditions. This formulation applies specifically to the stable crack growth period,

$$\frac{da}{dN} = C(K_{\text{max}} - K_{\text{min}})^m \tag{1.2}$$

where $\frac{da}{dN}$ is the increase in crack length per cycle and C and m are empirical constants. Several updates to this equation have been proposed such as the NASGRO equation [24], which incorporates stress ratio effects as well as defines a larger range of the fatigue crack life.

Experimental studies of the factors governing the crack growth rate have determined that parameters such as microstructure and mean load are relevant for varying growth rates (see e.g. [26]). Numerical simulations of fatigue crack growth remain slim. XFEM has been adapted to a fatigue framework capable of reproducing crack patterns and cycle lifetimes under complex loading (see [27], [28], [29]). Alternative

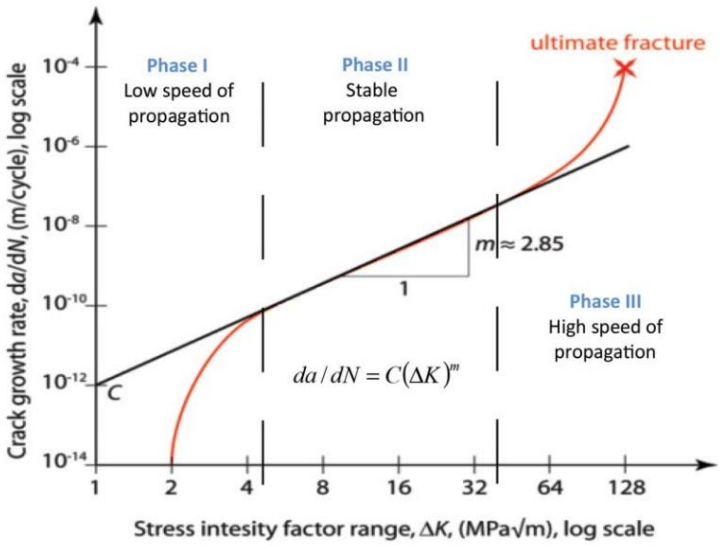

Figure 1.3: Visual depiction of fatigue crack growth life [25]

approaches such as peridynamics have also been adapted to simulate fatigue crack growth [30].

More recently, phase field models have been adapted to simulate fatigue growth. The basis of phase field fatigue models is the degradation of the fracture toughness with consistent variation in the elastic energy through a fatigue degradation function. Alessi et al. [31] proposes a 1D formulation that does degradation through accumulating equivalent strain. Carrara et al. [32] proposes a model that introduces the fatigue damage variable as an additional degree of freedom defined by an accumulative measure of elastic energy while demonstrating that an accumulating strain framework displays high mesh dependency at higher dimensions. This framework is demonstrated to reproduce Paris Law behavior and forms the basis of the models studied in this thesis. Utilizing this model, Ai et al. [33] simulates fatigue cracking in lithium-ion battery electrode particles. Simoes et al. [34] proposes a phase field model for the modeling of fatigue fracture in Shape Memory Alloys. Lo et al. [35] describes a fatigue model incorporating viscous damage dissipation that takes the Paris behavior of a material as an input. Loew et al. [36] simulates crack nucleation and growth in rubber due to fatigue. An alternative approach is proposed in [37], where the crack

driving force is bolstered with an additional fatigue term while sustaining the material toughness. The fatigue framework has also been extended to incorporate ductility (see e.g. [38], [39]) with such models used primarily to study low cycle fatigue.

In this thesis, two fatigue frameworks confined to high cycle fatigue considerations are simulated, where plasticity remains highly localized at the crack tip and may therefore be neglected, as opposed to low cycle fatigue, which would require the inclusion of plasticity. Both models are based on the degradation of the fracture toughness based on an accumulating fatigue damage variable. The crack closure model is based on the work in [32], where each cycle is applied individually through fluctuating boundary conditions. In contrast, the second approach functions through a representative load, with the fatigue damage variable evolving temporally, similar to creep boundary conditions.

1.3 Crack Growth Retardation

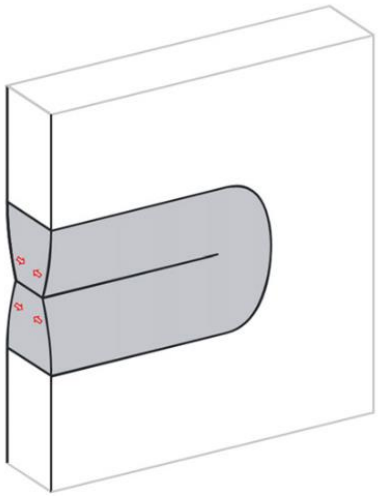

Figure 1.4: Illustration of how out of plane material flow in the plastic wake causes crack closure. [40]

In the 1970s, Elber [41] discovered premature surface contact between crack faces reached before the minimum loading condition, a phenomenon termed as plasticity induced crack closure. Single cycle overloads were found to cause significant retardation in the crack growth rate for subsequent cycles as a direct consequence of the

crack closure phenomenon. Since then various alternative sources of crack closure other than plasticity have been identified, such as roughness induced crack closure (see [40] for a review of these alternate phenomenon). They are not covered in the scope of this work.

Schijve [42, 43] considered residual stresses at the crack tip as a key feature responsible for crack growth retardation, acknowledging the difficulty in determining the individual influences of crack closure and residual stresses on the growth rate. [44] did not find crack closure to be a significant contributor to the overload effects, considering strain hardening and residual stresses to be a far more relevant contributor. Several supplementary micro-mechanical drivers of crack growth retardation have also been identified (see [45]).

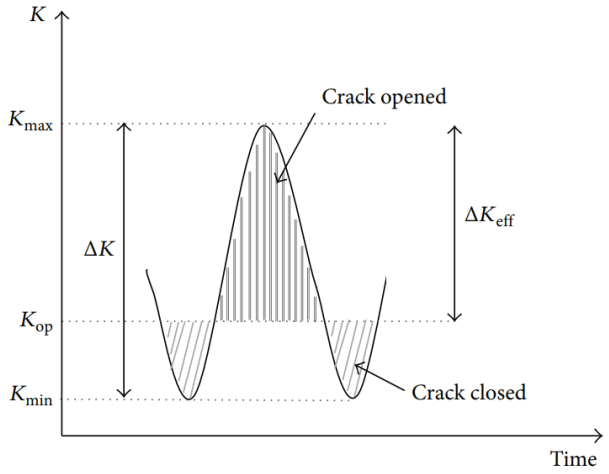

Figure 1.5: Visual representation of crack closure effects on the stress intensity factor range [46]

Analytical approaches are detailed in the literature to incorporate crack retardation due to the application of overloads. One style, based on the work of [41] involves the reduction of the stress intensity factor range, by replacing K_{min} with the stress intensity factor at crack opening K_{op}. Several proposals for calculating K_{op} are detailed in the literature (see e.g. [47, 46]), with the load ratio between the maximum and minimum loads acting as the controlling variable. When an overload is applied, K_{op}

is inflated in the region, causing a significant reduction in the stress intensity factor range which directly correlates to the crack growth rate.

An alternative approach is where the crack growth rate is altered according to the size of the yield zone around the crack tip. A plastic zone is present at crack tips at all times due to the high stress concentration. A single cycle overload significantly inflates this plastic zone. The way these models work is by retarding the crack growth rate based on the size increase in the plastic zone due to the overload. This retardation continues until the plastic zone begins to grow once more due to sufficient progression in the crack length. The Wheeler model [48] and Willenborg model [49] are notable examples.

The Wheeler model functions through the introduction of a retardation constant C_{p}, which reduces the crack growth rate upon the application of an overload, leading to the following re-interpretation of Paris' Law:

$$\frac{da}{dN} = C_{\mathrm{p}}.C(K_{\mathrm{max}} - K_{\mathrm{min}})^m. \tag{1.3}$$

C_p is influenced by the plastic zone size at the overload, as well as the crack length. It is described through the following formulation:

$$C_{\mathrm{p}} = (\frac{r_{\mathrm{pi}}}{r_{\mathrm{pOL}} + a_{\mathrm{ol}} - a_{\mathrm{i}}})^{\mu}. \tag{1.4}$$

The variables of this equation are described in Figure 1.6. This equation is applicable until the current plastic zone size crosses the overload plastic zone. μ is a material parameter calibrated from experiments.

It is important to not that the models introduced in the literature specifically pertain to framework based on the relation between the crack growth rate per cycle and the stress intensity factor. In contrast, the majority of phase field fatigue models are based on per cycle fatigue damage, hence a direct compatibility is difficult to establish. This thesis seeks to introduce the plasticity induced crack closure phenomenon and overload effects to the phase field paradigm without the explicit introduction of plasticity to the material model. This is done through the introduction of a novel fatigue dam-

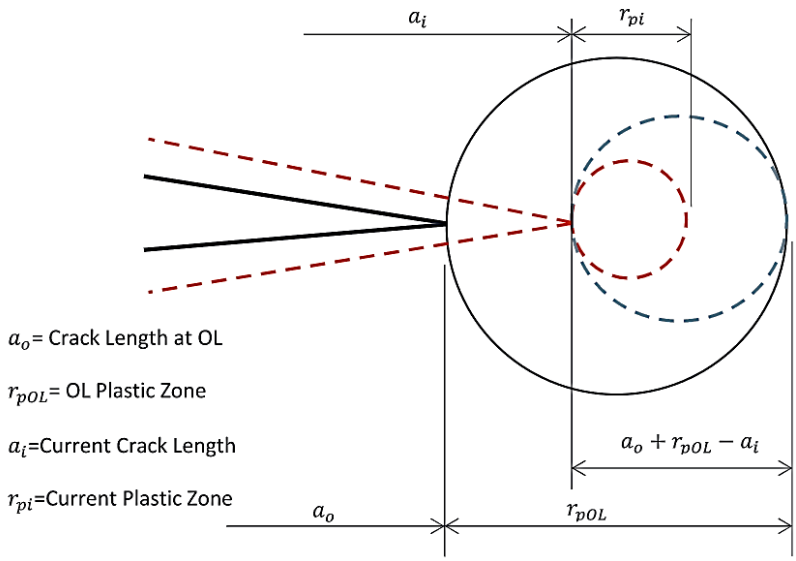

Figure 1.6: Visual representation of plastic zone evolution upon the application of an overload [29]

age threshold which evolves based on the loading history, simulating a reduction in the load range in which fatigue damage accumulates. In the second approach, a novel crack retardation framework similar to the Wheeler model is integrated into the model by describing a retardation zone at the crack tip based on the strain energy density distribution. Both models are designed to produce significant crack retardation upon the application of an overload, a phenomenon that has as yet not been explored in a phase field setting.

1.4 Ductile Fracture

It has been observed that ductile fracture in metals is driven by micro-mechanical mechanisms of void nucleation and growth [51, 52]. Several approaches have been proposed for the modeling of ductile fracture (see [53] for a review), capable of capturing the influence of factors such as the material temperature and the deformation rate.

Ductile damage models can be either coupled or uncoupled, with uncoupled models simply marking regions where a critical value representative of damage has been

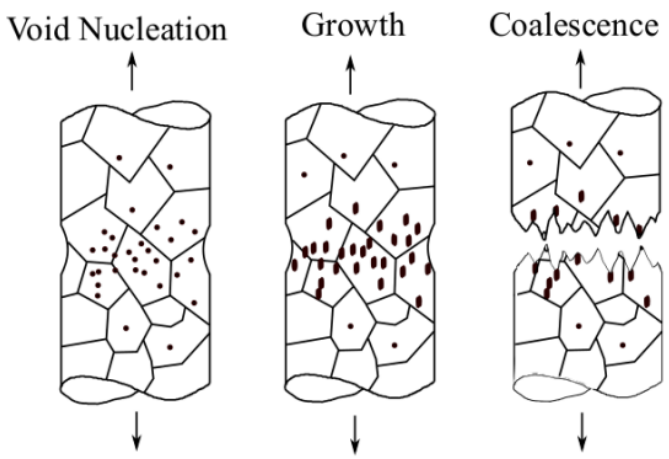

Figure 1.7: Stages of ductile fracture [50]

reached. Coupled models degrade the stiffness and stress carrying capacity of the material as damage is taken, allowing strain localization before fracture and hence producing far more realistic fracture behavior. Phase field models facilitate a mechanism for existing ductile damage models to be simulated in a coupled environment.

Furthermore, phase field models also incorporate non-local effects through a gradient term. Local material models assume that the response of a material depends only on the local state variables, while non-local models account for long-range interactions and the influence of gradient effects. Local models are known to demonstrate dependence on the mesh size [54] and utilizing non-local gradient based models allows mesh convergence [55] while also easing computational issues caused by strain localization [56]. In addition, the phase field model allows an implicit solution to plasticity, boasting far greater accuracy and advantages compared to a local, uncoupled explicitly simulated plastic damage model.

The micromechanical mechanisms of ductile fracture demonstrate a high dependency on the stress state characterized by stress triaxiality and Lode parameter (see [57], [58]). Ductile fracture models incorporating both parameters have been applied to numerical studies of metal forming (e.g. [59], [60]). Damage models such as the Johnson-Cook model [61] typically incorporate these effects through a cumulative measure to allow accurate predictions for fracture strains in ductile deformation cases

involving varying stress states. The Modified Mohr Coulomb (MMC) model is a ductile fracture model able to capture the evolution of plastic damage over a range of evolving stress states by considering both stress triaxiality effects and the influence of the Lode parameter (see [58]). Previous studies have attempted to incorporate stress dependent phenomenological models in ductile phase field paradigms. Borden et al. [62] incorporates stress triaxiality through the addition of a section of the Johnson-Cook damage model to the plastic damage accumulation. Li et al. [63] introduces a damage threshold that evolves with the MMC model. Vajari et al. [64] introduced a model that degrades the fracture toughness through the Stress-Weighted Ductile Fracture Model.

In the context of this thesis, the ductile phase field model's compatibility with the MMC damage model is demonstrated. This is done through an approach where the plastic damage is incrementally scaled through the MMC model. Furthermore, a plastic damage threshold is introduced to the model to control the onset of degradation following a critical strain value. While compatibility with the MMC model has been attempted before in [63], that approach was primarily through evolving the damage threshold with the MMC model, while this approach is relatively simpler, evolving the damage due to plastic deformation instead. Several benchmark specimens are simulated and experimental load-displacement curves are reproduced. The model's applicability in metal forming is also explored.

1.5 Aim of the Study

The aim of this study is to demonstrate the performance of the phase field methodology in the context of both fatigue fracture and ductile fracture. In terms of fatigue fracture, the goal is to introduce a phase field fatigue model capable of simulating experimental crack evolution curves and crack paths. Furthermore, the model should be able to produce the crack retardation effect when a single cycle overload is applied, which is an essential feature of fatigue behavior under variable amplitude loading. In terms of ductile fracture, the goal is to introduce a phase field ductile model that can reproduce experimental load-displacement responses and crack patterns for various benchmark specimens through the integration of the MMC model. This would allow

the use of existing calibrated MMC parameters within the phase field framework.

The organization of the thesis is as follows. Chapter 2 pertains to the foundations of the phase field fracture framework and its extension from brittle failure. The implementation of the model is discussed, where a UMAT is utilized through coupled temperature-displacement elements, where temperature acts as a stand in for the phase field parameter.

Chapter 3 concerns the extension of the phase field brittle model to a fatigue framework. Two separate approaches are considered. One approach calculates the fatigue damage taken per cycle and attempts to model retardation through a crack closure analogy, where an overload reduces the range of the load over which fatigue damage accumulates. The other approach accumulates fatigue damage through a representative load. Retardation is simulated through the integration of a zone-based retardation model that responds to overloads and scales down the fatigue damage at the crack tip.

Chapter 4 extends the brittle framework to a ductile setting through the introduction of a plasticity component to the crack driving force. The evolution of the plastic damage is controlled through a damage threshold and is scaled through the MMC model, allowing accurate material responses for a variety of stress states. The performance of the model is tested through various benchmark specimens and its applicability to forming operations is gauged through the simulation of the Nakajima test.

Chapter 5 summarizes the work covered in this thesis, key findings as well the scope for future work.

CHAPTER 2

PHASE FIELD MODELING OF BRITTLE FRACTURE

This chapter pertains to the theory behind phase field brittle fracture and the implementation on Abaqus, with the performance of the model tested through a CT-specimen. The theory behind the phase field fracture methodology is detailed. Following this, the numerical implementation of the model on Abaqus is described. A similarity between the steady state heat transfer equation and the phase field strong form is exploited to allow the use of coupled temperature-displacement elements with temperature acting as a stand-in for the phase field parameter. The merits of a phase field pre-crack versus a geometrically induced pre-crack are explored.

2.1 Foundations of Phase Field Fracture

The phase field method functions through the introduction of an additional degree of freedom ϕ, which in the context of fracture, represents a spectrum ranging of undamaged to completely fractured material. It is subject to the following restrictions:

$$\phi \in [0, 1] \qquad \dot{\phi} \geq 0. \tag{2.1}$$

In the context of this thesis, ϕ = 0, is taken to represent undamaged material, while ϕ = 1, represents complete fracture.

The foundations of fracture mechanics were laid by Griffith [4] more than 100 years ago, through the introduction of the following energy balance to describe crack evolution:

$$\frac{\partial E}{\partial A} = \frac{\partial \psi_{\mathrm{e}}}{\partial A} + \frac{\partial W_{\mathrm{s}}}{\partial A} = 0 \tag{2.2}$$

where E is the total energy of the system, ψ_{e} is the elastic potential energy and W_{s}

is the work done to create new surfaces during fracture. ∂A may be considered as the incremental change in the crack surface area. The term $\partial W_{\mathrm{s}}/\partial A$ is a characteristic constant for the material, referred to as the material's critical energy release rate. This may also be referred to as the material's fracture toughness in a phase field environment. The simplified implications of Griffith's energy balance are that a crack propagates when the elastic energy in the region reaches the fracture toughness, which is when it becomes energetically more favorable for the material to release its potential energy and form new surfaces.

Griffith's theory has it's own shortcomings, requiring the presence of a pre-existing crack and a well-defined crack path. These constraints are overcome through the introduction of the variational form of Griffith's energy balance [5],

$$E = E_{\mathrm{s}}(\Gamma) + E_{\mathrm{e}}(\Gamma, \boldsymbol{u}) \tag{2.3}$$

where E is the total energy of the system, E_{s} is the crack surface energy and E_{e} is the elastic potential energy. $\Gamma \subset \Omega$ represents the crack surface in the domain and is subject to the irreversibility condition $\dot{\Gamma} \geq 0$ which ensures that the crack surface cannot shrink and may only grow. The key assumption here being that the system evolves in a way to minimize the global energy of the system.

The following subsections cover how the phase field brittle fracture strong form is derived from the variational form.

2.1.1 Bulk energy and degradation function

The bulk energy E_{e} is a function of both the displacement field and the phase field. The displacement field contribution is interpreted through strain, while the phase field is represented by the parameter ϕ,

$$E_{\mathrm{e}} = \int \psi_{\mathrm{e}}(\phi, \boldsymbol{\varepsilon})\, d\Omega = \int g(\phi)\psi_0(\boldsymbol{\varepsilon})\, d\Omega \tag{2.4}$$

where, ψ_0 is the undegraded elastic energy. A linear elastic approach is applied in the scope of this thesis, leading to the following definition for ψ_0:

$$\psi_0 = \frac{1}{2}\boldsymbol{\varepsilon} : \mathbb{C} : \boldsymbol{\varepsilon}. \tag{2.5}$$

Meanwhile, $g(\phi)$ represents the degradation function, which serves as the main damage coupling actor in the phase field paradigm. Several options have been proposed in the literature for the degradation function, all of which are subject to similar constraints:

$$g(0) = 1 \qquad g(1) = 0 \qquad \dot{g}(\phi) \leq 0, \phi \in [0, 1]. \tag{2.6}$$

The most common degradation function in the literature is given as:

$$g(\phi) = (1 - \phi)^2 + k \tag{2.7}$$

where k is a nearly negligible constant (10^{-7} in our case), introduced to prevent singularities in the global stiffness matrix.

Since there are no thresholds for damage, ϕ evolves from the onset of loading, leading to premature degradation which essentially translates a non-linear elastic phase with steadily degrading stiffness. Several alternative degradation functions are proposed in the literature to achieve a more linear elastic phase. These include higher order degradation functions (see e.g. [62]) and parameterized families of functions (see e.g. [65]). The AT-1 model is an alternative phase field model that also enforces linear elasticity (see [66]).

2.1.2 Crack surface density function

The following approximation may be made for the crack surface energy:

$$E_{\mathrm{s}} = \int G_{\mathrm{c}}\, d\Gamma \approx \int G_{\mathrm{c}} \gamma\, d\Omega. \tag{2.8}$$

G_{c} is the fracture toughness of the material while γ is referred to as the crack surface density function, providing a description of the crack surface over the domain. This function is also responsible for the evolution of the phase field parameter in a way that produces a diffuse crack description. A geometric derivation of this function is described in [9] where they begin by considering the simplest 1-D case.

A fully opened crack at $x = 0$ is assumed with the phase field function $\phi(x)$ describing the crack surface. In a discrete crack description, $\phi = 0$ everywhere except at the crack surface where $\phi = 1$. In the diffuse crack description, the phase field may be represented through an exponential function $\phi(x) = e^{-|x|/l_0}$. Here l_0 is the length

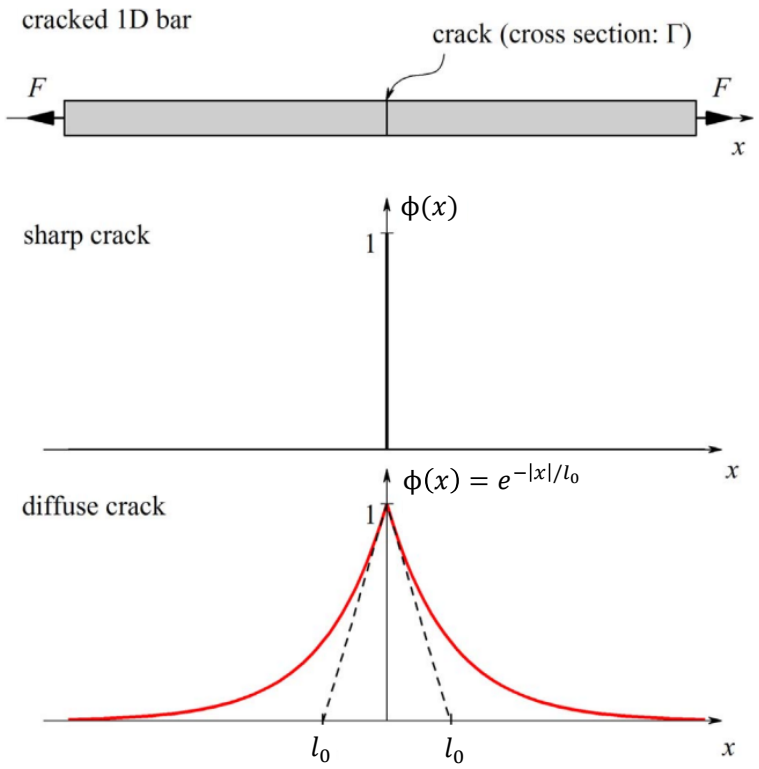

Figure 2.1: Discrete and diffuse crack descriptions in a 1-D case [67]

scale governing the diffuseness of the crack, with the sharp crack definition recovered as $l_0 \to 0$. The discrete and diffuse crack descriptions are visualized in Figure 2.1. For the boundary conditions $\phi(0) = 1$ and $\phi(\pm\infty) = 0$ this phase field function is a direct solution to the following differential equation:

$$\phi(x) - l_0^2 \phi''(x) = 0. \tag{2.9}$$

This differential equation, in turn, is the Euler equation of the variational principle, given a functional $I(\phi, \phi', x)$. In simpler terms, the solution $\phi(x)$ to the given differential equation with the given boundary conditions $W = \{\phi | \phi(0) = 1, \phi(\pm\infty) = 0\}$ minimizes the functional I,

$$\phi = \text{Arg}\{\inf_{\phi \in W} I(\phi)\} \tag{2.10}$$

where

$$I(\phi) = \frac{1}{2} \int_\Omega (\phi^2 + l_0^2 \phi'^2) dV. \tag{2.11}$$

This functional is constructed by integrating a Galerkin type weak form of Eq.2.9. With $dV = \Gamma dx$, if the functional I is solved for the given boundary conditions with the diffuse crack description at $x + 0$, the result is $I(\phi = e^{-|x|/l_0}) = l_0\Gamma$. Through rearrangement the fracture surface may be described as:

$$\Gamma(\phi) = \frac{1}{l_0} = \frac{1}{2l_0}\int_\Omega (\phi^2 + l_0^2\phi'^2)dV = \int_\Omega \gamma(\phi, \phi')dV. \tag{2.12}$$

It is seen that this is simply a scaled version of the functional I therefore the diffuse crack solution also minimizes this functional. The crack surface energy is essentially this very functional, with the additional G_c scalar term. Hence when the minimization problem of the functional is solved, while the bulk energy term drives the evolution of the phase field parameter, the crack surface energy term is directly responsible for the development of the diffuse crack distribution of ϕ. Adapted to higher dimensions, the following relation is found for γ, used in the context of this thesis:

$$\gamma = \frac{\phi^2}{2l_0} + \frac{l_0}{2}|\nabla\phi|^2. \tag{2.13}$$

The length scale parameter was initially introduced solely as a regularization parameter which governs the diffuseness of the crack, where $l_0 \to 0$ allows the crack surface to converge to Γ. Due to its influence on the ultimate tensile strength of a material, l_0 is treated as a material parameter akin to the material's internal length scale [68]. An alternative higher order formulation for γ is proposed in [69].

The energy functional is given as:

$$E(\phi, \boldsymbol{\varepsilon}) = \int g(\phi)\psi_0(\boldsymbol{\varepsilon})\, d\Omega + \int G_\mathrm{c}\gamma\, d\Omega. \tag{2.14}$$

Both the displacement field and the phase field are obtained as solutions to the minimization problem of this functional. This functional can be noted to resemble the format of the potential function for the Ginzburg Landau and Cahn Hilliard evolution equations, both of which relate to dual phase systems [70]. The functional E displays non-convexity in terms of both the displacement and phase fields simultaneously, but is convex with respect to each field individually with the other held constant [71].

By minimizing in terms of both the phase and displacement fields, the strong form of our problem may now be defined by the following set of equations:

$$\begin{aligned} &\nabla \cdot \boldsymbol{\sigma} = 0 \\ &G_\mathrm{c}(\ \tfrac{\phi}{l_0} - l_0\nabla^2\phi)\ - 2(1-\phi)\psi_0(\boldsymbol{\varepsilon}) = 0. \end{aligned} \tag{2.15}$$

2.1.3 Tensile Compressive Split

There are two major approaches to inhibiting compressive damage in the phase field paradigm, with both involving a split in the elastic energy. One approach involves the a volumetric-deviatoric split in the strain tensor, where only the deviatoric component is coupled with the phase field evolution (see [72]). An alternative approach (see [9]) proposes splitting the strain energy through the spectral decomposition of the strain tensor. This is the methodology employed in the scope of this thesis. In spectral form, the strain tensor is stated as thus:

$$\boldsymbol{\varepsilon} = \sum_i \varepsilon_i \cdot (\mathbf{n}_i \otimes \mathbf{n}_i) \tag{2.16}$$

The strain is then decomposed into its positive and negative contributions as follows:

$$\boldsymbol{\varepsilon}^{+} = \sum_i \frac{1}{2}(\varepsilon_i + |\varepsilon_i|) \cdot (\mathbf{n}_i \otimes \mathbf{n}_i) \tag{2.17}$$

$$\boldsymbol{\varepsilon}^{-} = \sum_i \frac{1}{2}(\varepsilon_i - |\varepsilon_i|) \cdot (\mathbf{n}_i \otimes \mathbf{n}_i) \tag{2.18}$$

The split strain energy contributions are functions of their respective strains $\psi_0^+(\varepsilon^+)$ and $\psi_0^-(\varepsilon^-)$. The energy functional is restated as thus:

$$E(\phi, \boldsymbol{\varepsilon}) = \int (g(\phi)\psi_0^+ + \psi_0^-)\, d\Omega + \int G_c \gamma \, d\Omega \tag{2.19}$$

As the negative strain energy contribution is uncoupled from the degradation, it no longer influences the evolution of the phase field. How the tensile-compressive split can influence the crack path distribution is visualized in shear conditions sample in Figure 2.2. The modified strong form now reads:

$$\begin{aligned} &\nabla \cdot \boldsymbol{\sigma} = 0 \\ &G_c(\, \tfrac{\phi}{l_0} - l_0 \nabla^2 \phi) \; - 2(1-\phi)\psi_0^+(\boldsymbol{\varepsilon}^{+}) = 0 \end{aligned} \tag{2.20}$$

2.1.4 Enforcing Irreversibility

One of the most essential requirements of the fracture model is the inability of the fracture surface to 'heal', enforced here by the condition $\dot{\phi} \geq 0$. This is achieved

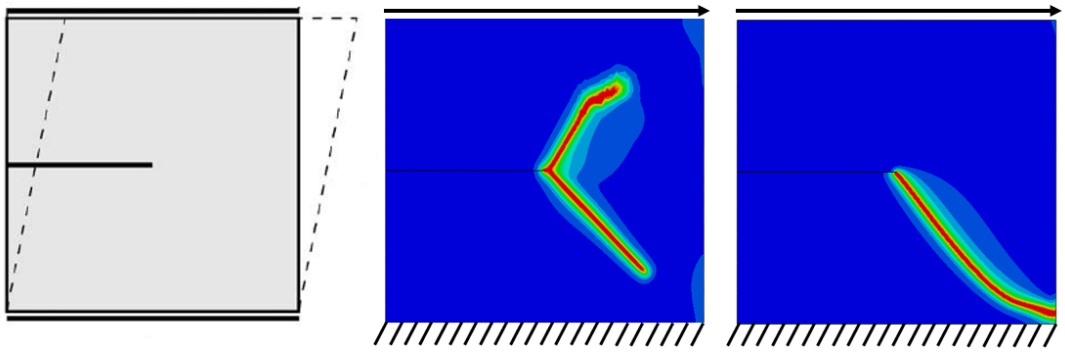

Figure 2.2: Crack path under shear conditions without tensile-compressive split (center) and with tensile-compressive split (right)

through the introduction of a local history variable H, based on the approach introduced by [9]. H is defined as follows:

$$H = \max_{\tau \in [0,t]} \psi_0^+(\tau) \tag{2.21}$$

This represents the maximum tensile elastic energy achieved throughout the loading history and acts as the central driving force of crack growth, leading to the following version of the strong form:

$$G_c(\frac{\phi}{l_0} - l_0 \nabla^2 \phi) \ - 2(1-\phi)H = 0 \tag{2.22}$$

2.2 Numerical Implementation

All numerical simulations are conducted over the Abaqus interface using user material (UMAT) subroutines. The inbuilt implicit finite element solver is employed. Due to there being no pre-defined coupled displacement-phase field elements present in the system, two options are available. One being the use of a user defined element (UEL) subroutine, which allows the definition of coupled displacement-phase field elements (see e.g. [67]). The alternative is to use coupled temperature-displacement elements with temperature behaving as a stand-in for the phase field parameter, by exploiting a similarity between the phase field paradigm strong form and the steady state heat transfer equation (see e.g. [73]). This thesis employs the latter approach.

Rearranging the strong form of the brittle problem allows a comparison with the heat

transfer equation,

$$\begin{aligned} k\nabla^2 T &= -r \\ \nabla^2\phi &= \frac{\phi}{l_0^2} - 2(1-\phi)\frac{H}{G_c l_0} \end{aligned} \tag{2.23}$$

Setting material conductance k to 1, a heat source is introduced in model through the additional HETVAL subroutine,

$$r = -(\frac{\phi}{l_0^2} - 2(1-\phi)\frac{H}{G_c l_0}) \tag{2.24}$$

Such a framework is sufficient in simulating brittle fracture with the temperature field representing the phase field. It allows the use of the inbuilt mechanisms of Abaqus, rather than reducing it to a solver. Describing a pre-crack through the phase field rather than a geometric crack may be done through a temperature boundary condition applied in a step preceding the loading step. The performance of pre-cracks applied through the phase field rather than geometric features in a brittle environment, has been explored in preceding studies [74].

Further alterations to the brittle model to incorporate plasticity or fatigue are introduced through the H and G_c terms respectively. Non-linear geometric effects are incorporated in the ductile simulations due to the high deformations involved. This is deemed unnecessary for the fatigue simulations.

For the fatigue simulations, a python script is developed to track the evolution of the crack length over the simulation time. Phase field value at the FE nodes is tracked throughout the body, with a threshold value of 0.9 confirming that the crack has reached the co-ordinates of a node.

A staggered solution approach is employed to facilitate easier convergence (see e.g. [67]). In such a scheme, the displacement field and the phase field are solved for separately per increment, with the displacement field solution from the previous increment driving the phase field solution in the current increment and the phase field solution from the previous increment driving the current increment's displacement field solution. The downside of this approach is that the framework is not unconditionally stable. Therefore the increment size must be sufficiently small to confirm the reliability of the solution. As observed in the results in Figure 2.3, a low number of increments causes a diffused inaccurate solution, while by decreasing the increment size within an identical solution time, the phase field distribution converges to

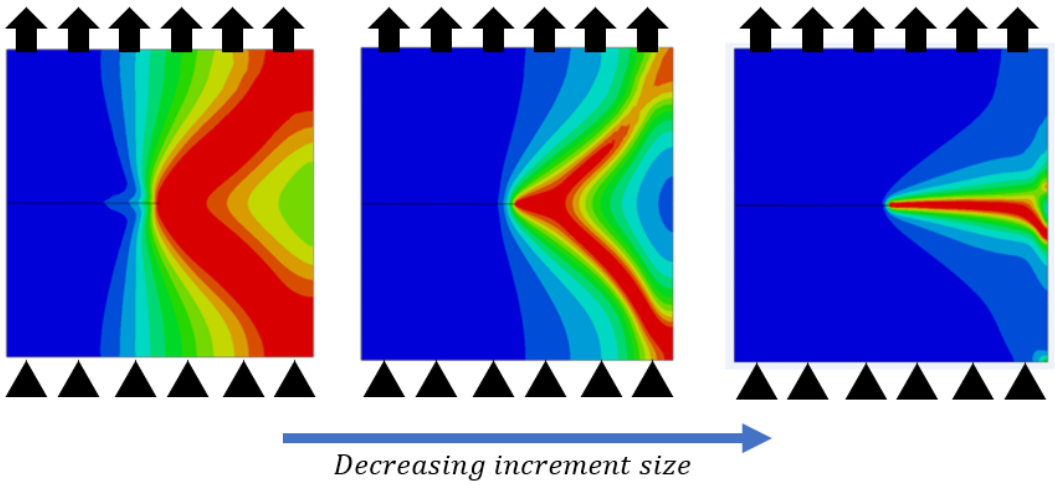

Figure 2.3: The influence of incrementation on the phase field in a staggered solution scheme

an accurate result.

A downside of using a UMAT over a UEL, particularly in the context of fatigue, is that we lose access to quasi-Newton solvers which allow the use of a monolithic solution scheme, removing the conditional stability problem. Quasi-Newton monolithic solution schemes have been demonstrated to have several scales lower computational costs than traditionally used staggered schemes (see e.g. [13, 75]). This option is not available for coupled temperature-displacement problems and hence is only available with a UEL.

2.3 Geometric vs. Phase Field Pre-Crack

This section concerns the behavior of the model in monotonic loading cases. A 2D CT model is studied to analyze the effectiveness of the fatigue model. Plane strain conditions are assumed. The model dimensions are taken from [76]. The model thickness is taken as 2.5mm. The element type is CPE4T.

A pre-crack is applied to the model of length 10mm. Two methodologies are available for applying this crack, hence model performance of the geometric pre-crack is compared to the phase field pre-crack in both fatigue and monotonic loading cases.

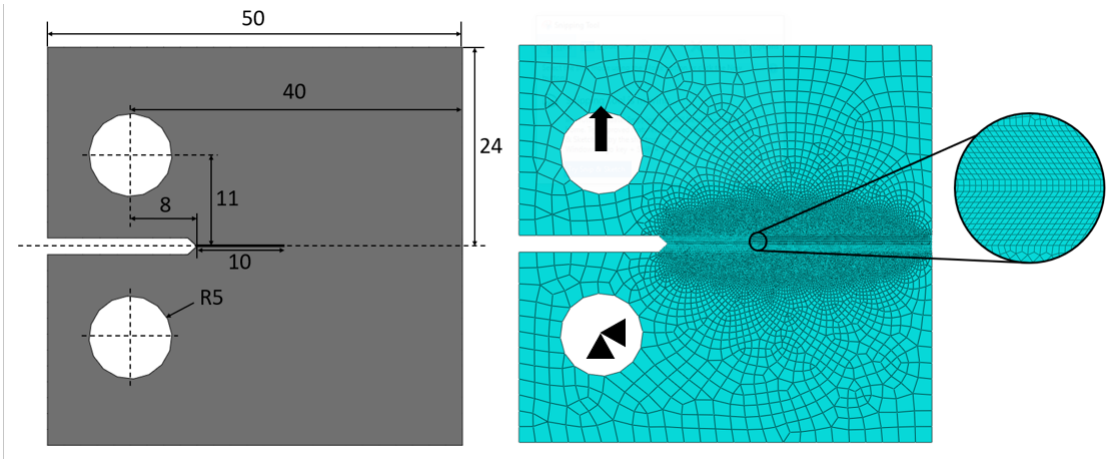

Figure 2.4: Dimensions of the CT specimen

In the case of the geometric pre-crack, its application is done through splitting nodes through the seam condition in Abaqus. The phase field pre-crack is applied through a temperature boundary condition, where a temperature of 1 is applied to a set of elements representing the pre-crack.

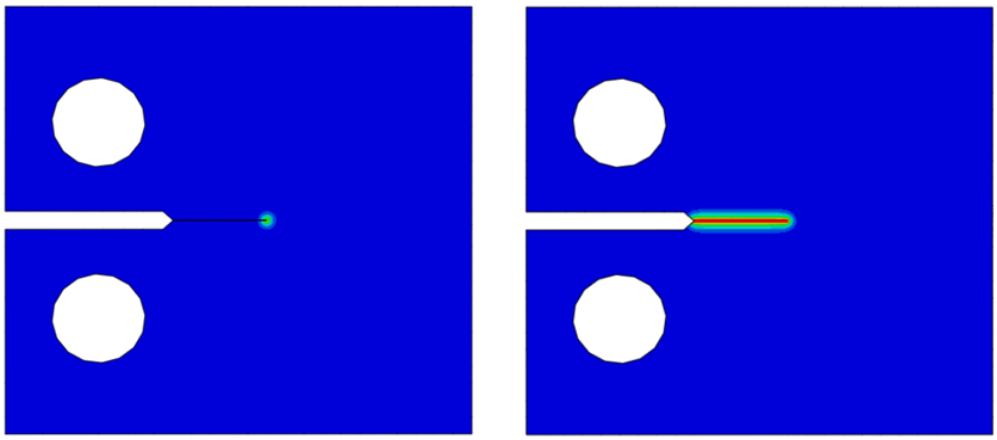

Figure 2.5: Geometric pre-crack(left) and phase field pre-crack(right)

The specimen is restricted from the lower hole in the x and y directions, while rotation is permitted. This is done through a kinematic coupling between the perforation wall and a centered reference point, to which the boundary conditions are applied. A similar coupling is performed for the upper hole to a separate reference point to which the loading is applied. A displacement in the y direction is applied to cause the model to fracture completely and displacement in the x-direction is restricted. A

displacement boundary condition is preferred over a traction boundary condition in the monotonic loading case to be able to observe complete fracture, as in the case of a traction boundary condition, the model can no longer converge the moment the model becomes unable to carry the applied loading. The mesh is made finer along the expected crack path, with a size of 0.1mm. The material parameters are tabulated in Table 2.1.

E (MPa)	Poisson's Ratio	Length Scale(mm)	G_c(N/mm)
194,000	0.3	0.5	5

Table 2.1: Material parameters for QSTE340TM steel

The elastic parameters for QSTE340TM steel are taken from [76]. The phase field parameters are roughly calibrated to produce fracture within the required loading period. The fracture toughness is kept low to produce brittle fracture at a reasonable strain. This value is later inflated for the fatigue simulations.

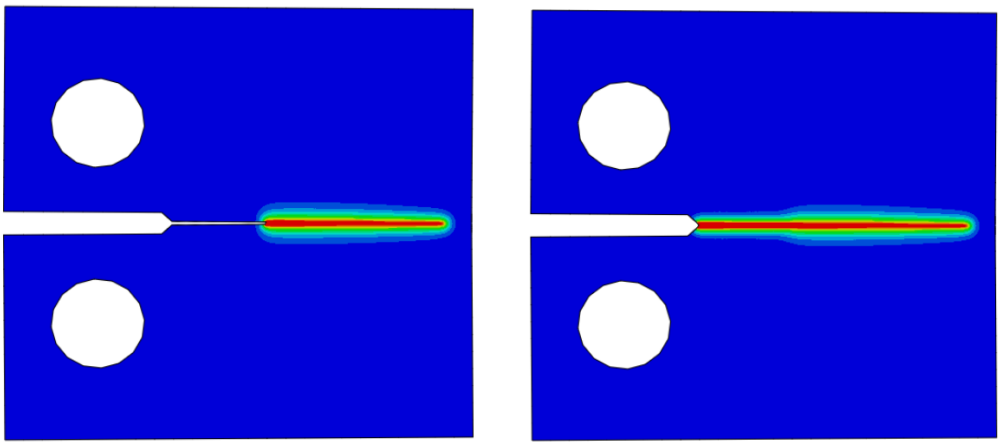

Figure 2.6: Geometric monotonic loading crack (left), phase field monotonic loading crack (right)

The crack distribution for both types of pre-cracks is observed to be identical as visualized in Figure 2.6. However, while both fractures occur at identical strains, the geometric pre-crack achieves a slightly higher maximum load. This can be observed in the load-displacement curves for both cases plotted in Figure 2.7. Previous studies have explored the performance of a geometric pre-crack versus a phase field pre-crack

(see [74]), where the geometric pre-crack is found to inflate the fracture toughness. Hence the results are corroborated. Building on this finding, both geometric and phase field pre-cracks are studied in a fatigue environment in the following chapter.

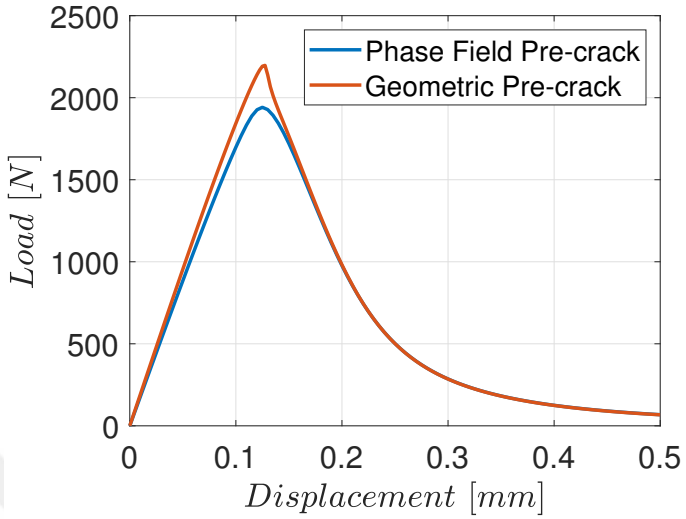

Figure 2.7: Load-Displacement responses for both geometric and phase field pre-cracks (static loading)

CHAPTER 3

PHASE FIELD MODELING OF FATIGUE FRACTURE UNDER VARIABLE AMPLITUDE LOADING

In this chapter, two distinct approaches to modeling fatigue are explored and simulated. They are corroborated with experimental data to gauge the models' ability to capture crack paths as well as crack retardation effects due to overload. Isotropic linear elastic materials are considered exclusively and crack tip plasticity is neglected. One approach involves the simulation of crack closure effects through the introduction of a fatigue damage threshold that evolves with the loading history of the material. The second approach evolves the fatigue damage through a representative load and introduces a zone-based crack growth retardation framework that scales the fatigue damage through a retardation parameter, following the application of an overload. FE fatigue simulations are conducted over Abaqus and overload results are compared to experimental crack evolution data from [76, 77]. Crack path studies are conducted for both models for an asymmetric 3-point bending test and results are compared to the experimental data from [78].

3.1 Extension to Fatigue

Following the recommendations of the bulk of the literature, fatigue effects are incorporated in the brittle phase field model through the degradation of the fracture toughness over the course of the loading period. To this end, an additional fatigue degradation function is introduced to the strong form,

$$f(\alpha)G_{\mathrm{c}}(\frac{\phi}{l_0} - l_0\nabla^2\phi) - 2(1-\phi)H = 0. \tag{3.1}$$

Certain options for fatigue degradation functions are proposed in the literature. Alessi et al. [31] introduces a logarithmic fatigue degradation function capable of reproducing Wöhler curves. Carrara et al. [32] demonstrates that their framework naturally recovers Paris' Law, which is the fatigue degradation function used in this study, defined as follows:

$$f(\alpha) = \begin{cases} 1 & \text{if } \alpha \leq \alpha_{\mathrm{T}} \\ \left(\dfrac{2\alpha_{\mathrm{T}}}{\alpha + \alpha_{\mathrm{T}}} \right)^{n} & \text{otherwise} \end{cases} \tag{3.2}$$

where α_{T} is a the threshold fatigue damage which must be exceeded before degradation to commence. In physical terms it may be said to represent a phase of plastic instability before the appearance of micro-defects. Meanwhile α is an additional damage parameter representing the accumulation of fatigue damage over the deformation history. The exponent n of the fatigue degradation function is taken as 2 by [32] and this value is retained in the thesis unless stated otherwise. This exponent is later demonstrated to control the concavity of the crack life curve. Two different models are compared and implemented in this study, with their behavior controlled through the definition of α and its accompanying boundary conditions. Their respective features are highlighted in the following sections.

3.2 Simulating fatigue with crack closure effects

In this approach, crack retardation is simulated through modeling crack closure without the explicit incorporation of plasticity. α is described as:

$$\dot{\alpha} = \begin{cases} g\dot{\psi}_0 & \text{if } \dot{\psi}_0 \geq 0 \\ 0 & \text{otherwise.} \end{cases} \tag{3.3}$$

Hence fatigue damage only evolves during the loading stage, with no damage taken at unloading and at the point of complete failure, no further damage accumulates. In [31], the fatigue damage variable is taken as a measure of accumulating strain, which would perhaps serve as a better comparison of fatigue damage with classical models that are governed through the stress intensity factor. However, in [32], it is shown that a strain based fatigue damage variable demonstrates high mesh dependency, whereas a deformation energy based fatigue damage variable performs far better. Hence the

latter approach is preferred in this thesis.

The implementation of this model involves the application of a fluctuating load boundary condition, with each cycle modeled individually. This however, raises the complication of applying cycles in the order of 10^6. Some scaling in fatigue simulations through an accumulating damage methodology is inevitable.

The obvious approach to modeling plasticity induced crack closure may at first glance seem to be the inclusion of plasticity in the fatigue model. There are however, several reasons why such a model may not perform our required function. Crack closure stems directly from the interaction between crack surfaces but the diffuse crack model has no discontinuous surfaces marking the crack region. Furthermore, in the case of high cycle fatigue, there is highly localized plasticity at the crack tip, functioning at scales that would only create unnecessary computational headaches.

The alternative approach chosen in this thesis is to have the effects of plasticity felt without explicitly changing the material model, through the fatigue damage evolution. This limits the application of this model to high cycle fatigue, where plastic effects are highly localized at the crack tip and may be neglected. Inspiration is sought from existing formulations for the incorporation of crack closure effects detailed in the literature, with the fundamental approach involving inflating the stress intensity factor at the minimum load.

There are several approaches detailed in the literature to define the effective stress intensity factor range ΔK_{eff} by replacing K_{min} with the stress intensity factor at crack opening K_{op}. [79] proposes the following function to define the effective stress range:

$$\frac{S_{\text{max}} - S_{\text{op}}}{S_{\text{max}} - S_{\text{min}}} = 0.5 + 0.4R \tag{3.4}$$

where R is the stress ratio given by $\sigma_{min}/\sigma_{max}$ where these are the min and max load stresses. In this proposal, a higher stress ratio actually inflates the effective range.

Our preliminary work [80] takes inspiration from the following proposal [81],

$$\frac{K_{\text{op}}}{K_{\text{max}}} = 0.45 + 0.22R + 0.21R^2 + 0.12R^3. \tag{3.5}$$

[82] for zero-based loadings, proposes the following measure:

$$\frac{K_{\text{op}}}{K_{\text{max}}} = 0.557. \tag{3.6}$$

While noting that K_{op} would inflate for higher stress ratios. A reduction of the damage range is the key feature of the crack closure approach and these models hint at the order by which the damage threshold should be defined. The fatigue damage is defined in energy terms and so a fatigue damage threshold that varies linearly with the maximum deformation energy history H is introduced,

$$H_{\text{ft}} = k_{\text{ft}} H \tag{3.7}$$

where $k_{\text{ft}} \in [0, 1]$. A direct dependence on the local history variable is established and the linear co-efficient may be re-calibrated for different material conditions. The evolution equation for the fatigue damage variable is now defined as the following:

$$\dot{\alpha} = \begin{cases} g\dot{\psi}_0 & \text{if } g\psi_0 \geq H_{\text{ft}} \text{ and } \dot{\psi}_0 \geq 0 \\ 0 & \text{otherwise.} \end{cases} \tag{3.8}$$

Hence, fatigue damage is only taken while the material's strain energy density exceeds a threshold defined through the local history variable. In our previous work, this formulation was found to successfully reproduce crack retardation when overloads were applied. The fundamental idea remains the same as that of preceding literature: a reduction in the range of loading over which fatigue damage is taken. The algorithm is visualized in Figure 3.1.

3.2.1 Geometric vs. Phase Field Pre-Crack in a fatigue environment

To see if the pre-crack type influences the crack life in a fatigue environment, the CT specimen from the previous chapter is considered once more. A fluctuating load of 2 kN is applied to the upper hole reference point with a load ratio of 0.1. All other boundary conditions are kept identical. The fracture toughness G_{c} is inflated to 300 N/mm. The fatigue threshold parameter k_{ft} is set to 0.6 and the fatigue damage threshold α_{T} is taken as 30. Both pre-crack types are tested. The results are visualized through crack length vs. cycles curves in Figure 3.2. It is found that the disparity in the crack life is minimal, implying that either option is acceptable in a fatigue

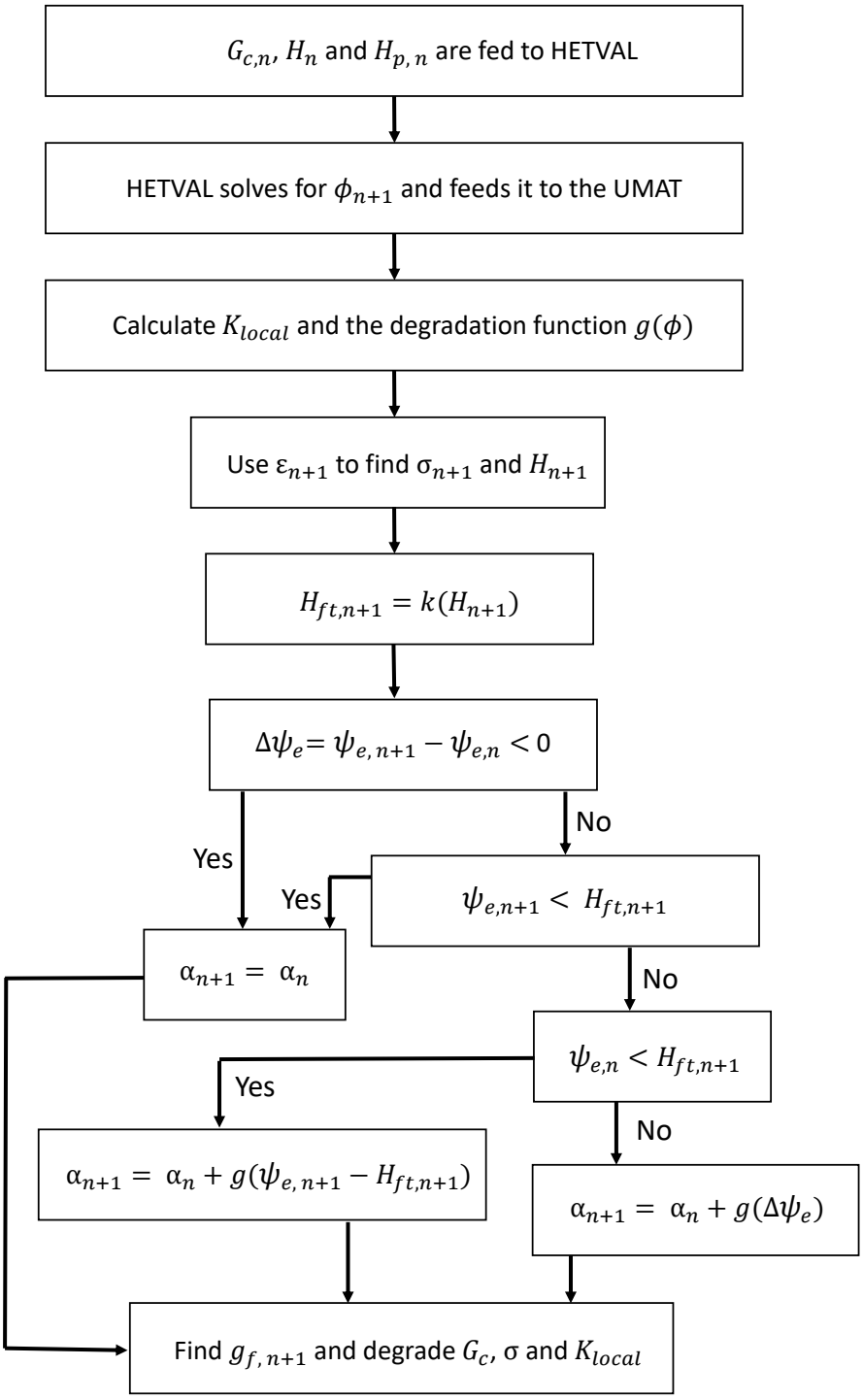

Figure 3.1: Crack closure fatigue model algorithm visualized

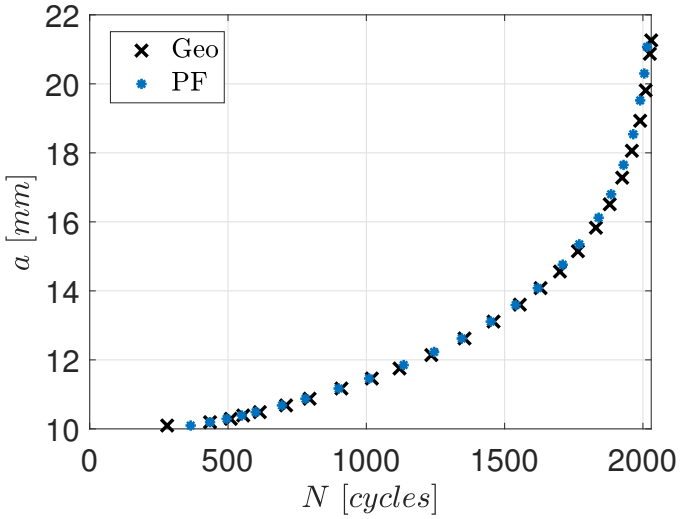

Figure 3.2: Crack life for both geometric and phase field pre-cracks (fatigue loading)

paradigm. This is because the crack life is more strongly governed by the fatigue threshold α_{T}, so small fluctuations in the fracture toughness are insignificant.

3.2.2 The influence of the fatigue damage threshold on crack life

The influence of H_{ft} on the crack growth rate is explored to see how this additional feature affects the model. A comparison with the experimental results of [76] is made. To save computational time, a pre-crack is defined through the phase field, so that only the relevant crack growth period may be studied.

A higher fatigue threshold constant translates to a lower range over which fatigue damage is taken, therefore slowing down the crack growth rate, as visualized in Figure 3.3.

The overload capabilities of the model are also tested for various definitions of H_{ft}. Single cycle overloads are applied when the crack length reached 12mm. Overload ratios of 1.5 and 2 times the maximum load are tested. The results are visualized in Figures 3.4, 3.5, 3.6 and 3.7.

A higher linear exponent for H_{ft} is found to directly translate to stronger crack growth retardation for the same applied overload levels. Higher overloads are observed to

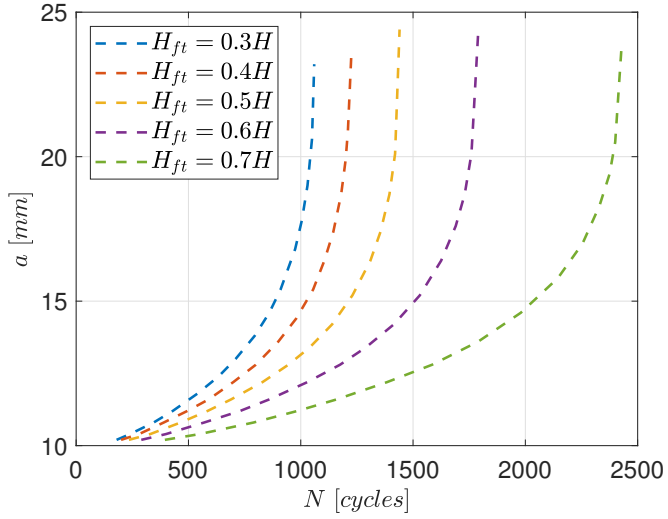

Figure 3.3: Crack length vs. cycles visualized for various fatigue threshold definitions

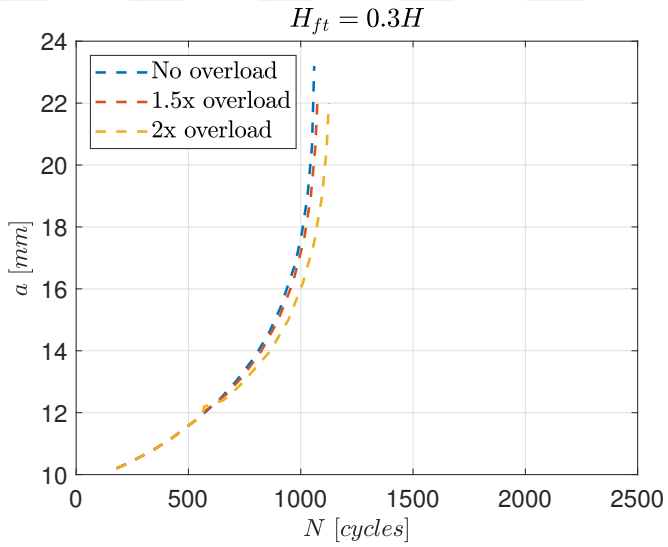

Figure 3.4: Crack Evolution for $k_{\text{ft}} = 0.3$

produce greater crack retardation effects, which is consistent with the experimental literature (see e.g. [83]). Furthermore, the model naturally recovers the life gain comparison between 1.5 and 2 times the overload, with the latter having a far more significant influence on the crack life. At $k_{\text{ft}} = 0.7$ crack arrest occurs. This model is unable to reproduce experimental levels of life increase due to applied overloads, which are quite higher. This is a serious limitation for this model and may be explained by the fact that crack closure has not been deemed to be the sole contributor

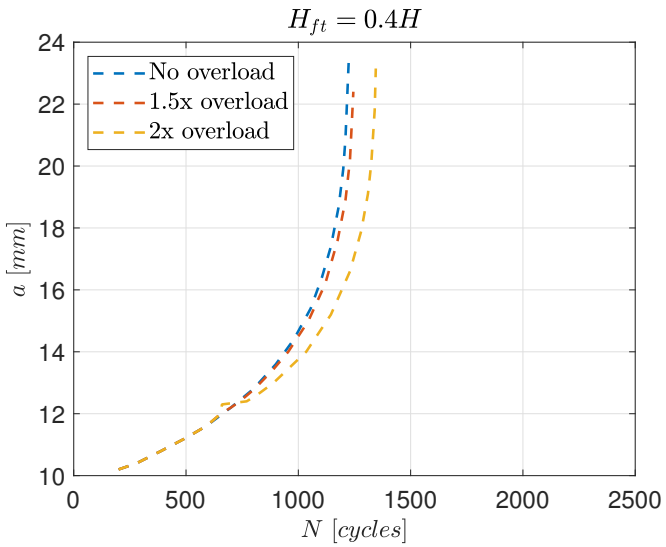

Figure 3.5: Crack Evolution for $k_{\text{ft}} = 0.4$

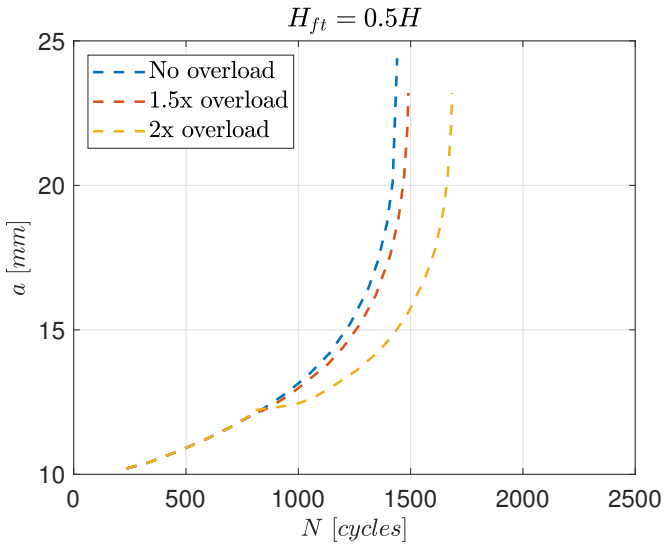

Figure 3.6: Crack Evolution for $k_{\text{ft}} = 0.5$

to crack retardation, with residual stresses at the crack tip also having a significant role in smothering the damage being taken per cycle. A more effective version of this model could eventually take this effect into account.

It is found that the crack growth can be scaled to a lower number of cycles by reducing the fatigue threshold or the fracture toughness. However, it is still recommended that the number of cycles be kept as high as possible. This is because, each singular cycle in the scaled simulation represents a batch of experimental cycles. This

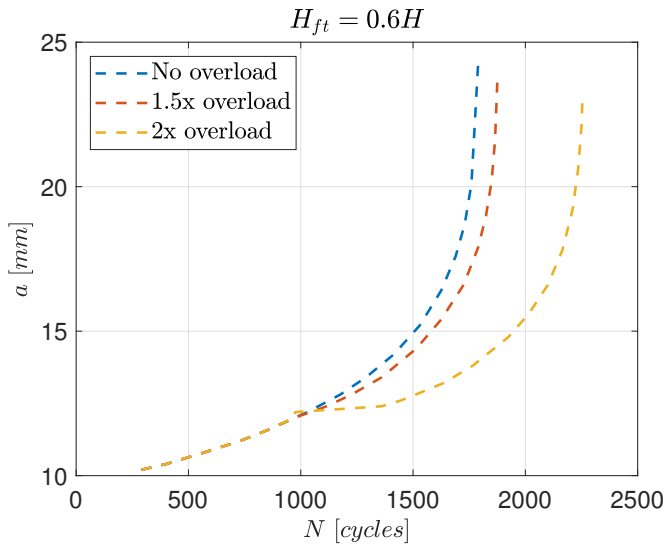

Figure 3.7: Crack Evolution for $k_{\text{ft}} = 0.6$

becomes particularly relevant while studying overload, where single cycle overload experimental results become difficult to reproduce, with the overload cycle having a very high contribution to the crack growth.

3.2.3 Three point notched bending test with asymmetric perforations

The ability of the model to accurately capture experimental crack paths is tested through a 3-point bending test with asymmetric perforations. The specimen is visualized in Figure 3.8. Material properties from the previous subsection are utilized. Simulated crack paths are compared to the experimental works of [78].

A fluctuating displacement is applied in line with the center line of the specimen. The point loads at the boundary conditions and loading zone are found to behave as stress concentrators, attracting crack growth rather than the notch tip. To prevent this, the phase field model is applied to a restricted region through which the crack was expected to propagate, with an identical linear elastic model applied to the rest of the region. The mesh is refined in this region.

Three different crack location and size combinations are studied in cases with perforations and without. The relevant dimensions particular to these cases are tabulated in Table 3.1. Type A cases designate the absence of perforations and Type B are cases

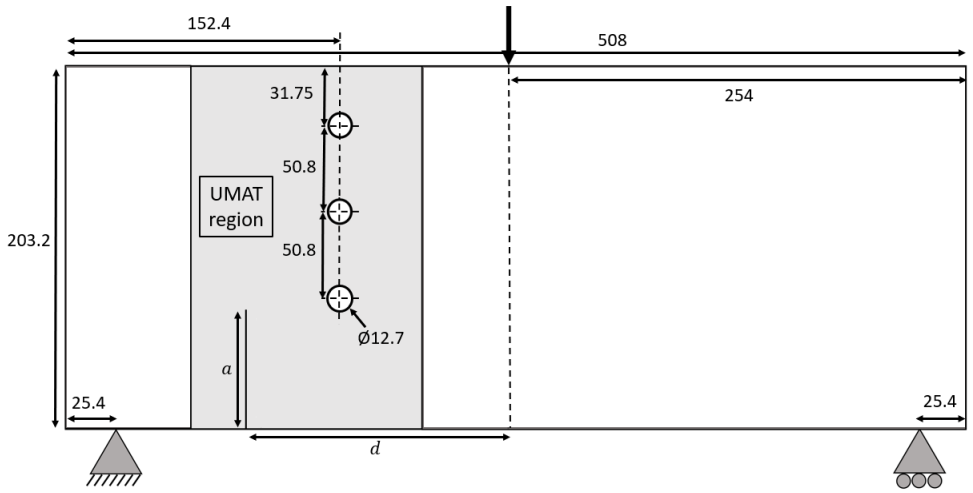

Figure 3.8: 3 point bending specimen

	Case 1	Case 2	Case 3
Crack Length 'a' (mm)	63.5	38.1	25.4
Crack Location 'd' (mm)	152.4	127	152.4

Table 3.1: Crack size and location for the studied cases

with them present.

3.2.4 Fatigue and brittle cases crack path comparisons for Type A cases

While the primary purpose of this study is to model complex high cycle fatigue behavior in ductile materials, a comparison may be drawn with the crack paths for a brittle framework applied to an identical model with identical boundary conditions as fatigue and brittle crack paths are known to coincide.

All three cases are implemented in the both the brittle and fatigue fracture models to study the correlation between crack paths. The results have been visualized in Figures 3.9 and 3.10. The static cases are conducted over 1000 increments, while the fatigue cracks are grown over 200 cycles consisting of 1400 increments. The boundary conditions are applied to ensure that fracture occurs firmly in the latter half of the simulation.

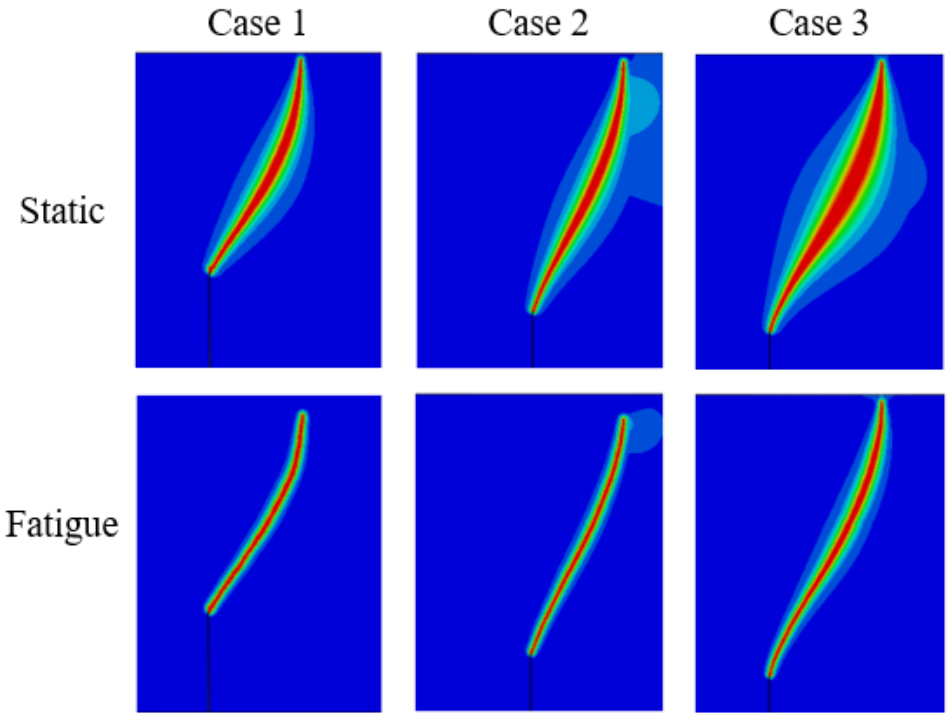

Figure 3.9: A-type static(up) and fatigue(down) crack path comparisons

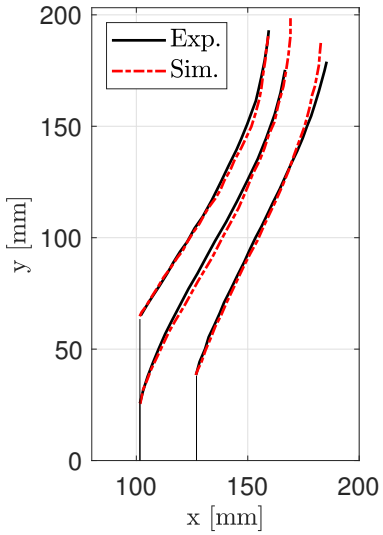

Figure 3.10: Crack path comparison between experimental and fatigue results

A rather immediate comparison that may be drawn between the fatigue and static crack results is that while their crack paths correspond, the fatigue phase field distribution is noticeably less diffuse. As noted in our preliminary work, this may attributed

to the fact that the fatigue damage distribution adds an additional localization, as well as the fact that in fatigue crack growth, the evolution of the phase field is spread out more evenly over the increments, in comparison to the static case where crack growth happens over a very small percentage of increments over the entire deformation. In essence, the fatigue case may be said to overcome the unconditional instability of the staggered solution scheme far more effectively, leading, allowing a tentative suggestion that the phase field paradigm is more suited to fatigue failure rather than brittle failure.

3.2.5 Type B convergence study

Perforations added complications to the simulation, serving as stress concentrators that draw the crack in. Hence the cases with perforations are considered suitable to conduct a convergence study.

Three features of the model are studied to determine their influence on crack path evolution. These are the length scale l_0, the number of increments over which the crack propagates as well as the mesh size. The mesh is refined only in the area through which the crack is expected to propagate for computational ease. The parameter sets that are studied are stored in Table 3.2 where the total increments cover the total growth of the crack. Case 1B is studied and the results visualized in Figure 3.11 are used as the basis of the convergence study.

The influence of each of the three parameters may now clearly be observed. The pattern in all three cases is rather predictable, with a smaller length scale, a finer mesh and a larger number of increments producing a better solution. According to recommendations, the length scale should be at least twice the size of the mesh to minimize the influence of the mesh distribution over the crack path [67].

Simulation 8 is uses the most computationally expensive parameter set with no significant improvement from the Simulation 1 parameter set, therefore it is assumed that convergence is sufficiently achieved.

It is plain to see the computational complications that would be involved in capturing the correct crack path in the brittle case where the crack growth occurs over a limited

Simulation No.	Length Scale (mm)	Mesh Size (mm)	Total Increments
1	1	0.5	10500
2	1	0.5	5000
3	1	0.5	18600
4	1	1	20000
5	1	0.3	9450
6	2	0.5	9800
7	0.8	0.5	9800
8	0.8	0.3	16940

Table 3.2: Parameters of the cases involved in the convergence study

percentage of the total increments. While doable in theory, in practice it is a computational headache, requiring prior knowledge of the time frame during which the crack propagates to allow heavy increment size refinement.

3.2.6 Fatigue and brittle cases crack path comparisons for Type B cases

When studying the crack paths for cases that include perforations, the difference in performance of both the brittle and fatigue paradigms becomes far more stark. In each of the three brittle cases, the crack deviates from experimentally determined paths and is drawn into the perforations. In contrast, the fatigue paths are found to correspond to the experimental paths in two of the three cases. The results are visualized in Figures 3.12 and 3.13.

Case 1B and 3B have previously also been captured in a brittle setting [84] but with a highly refined mesh, small length scale and a very high number of increments, the computational requirements of which were considered too challenging in the context of this thesis. In contrast, the fatigue model could capture these results with parameters that have a relatively lower computational cost. Case 2B proves to be difficult to capture even under fatigue conditions. Lowering the length scale and mesh size does improve the solution, implying that there may be a convergent point where the phase field fatigue model could capture this crack path. However, the computational

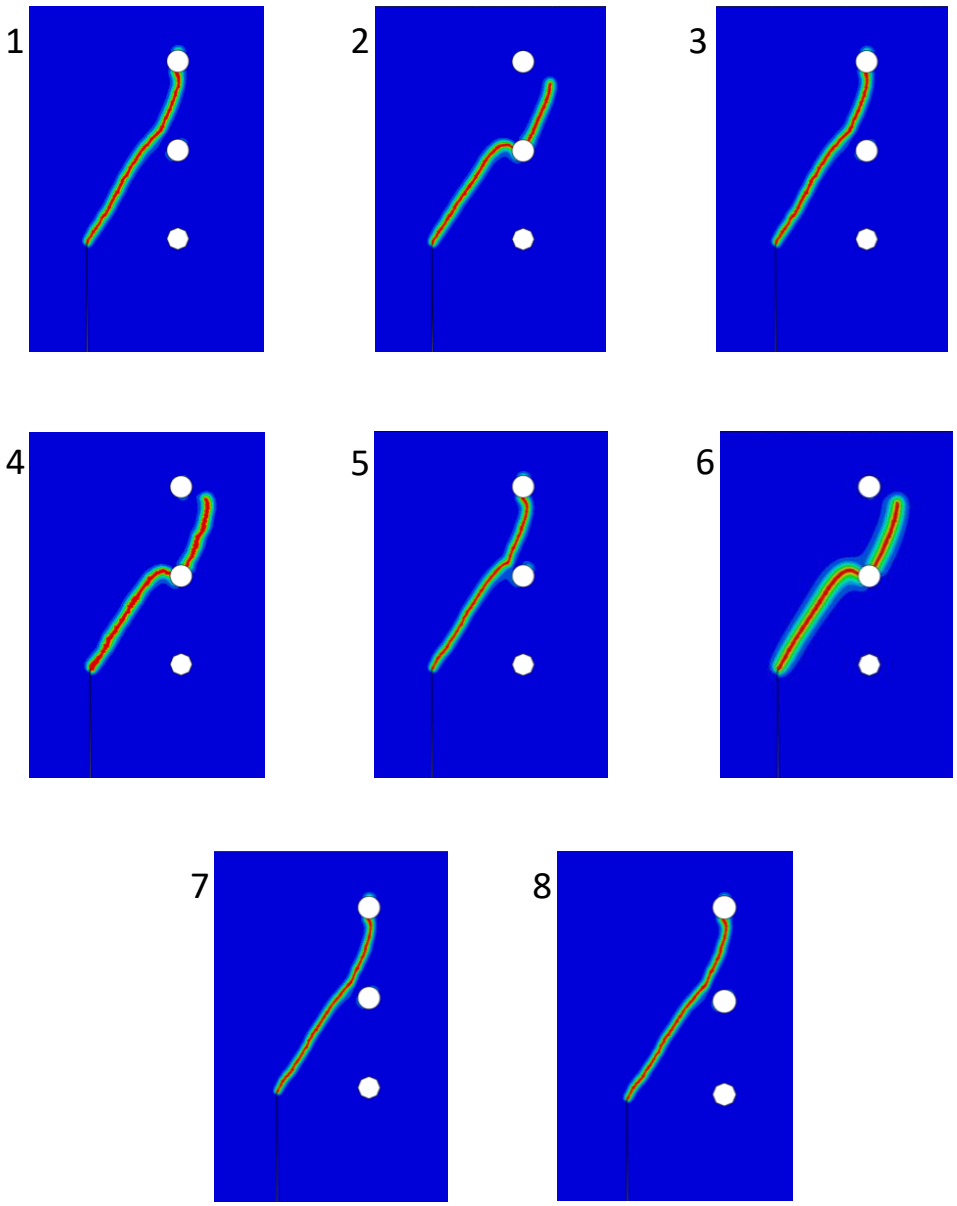

Figure 3.11: Case 1B crack paths for various parameter sets

requirements put that in question. This case is a rather excellent demonstration of the limitations of the phase field paradigm.

One of the issues with modeling fatigue fracture by applying each cycle individually, is that it is not computationally feasible to apply a realistic number of cycles in the

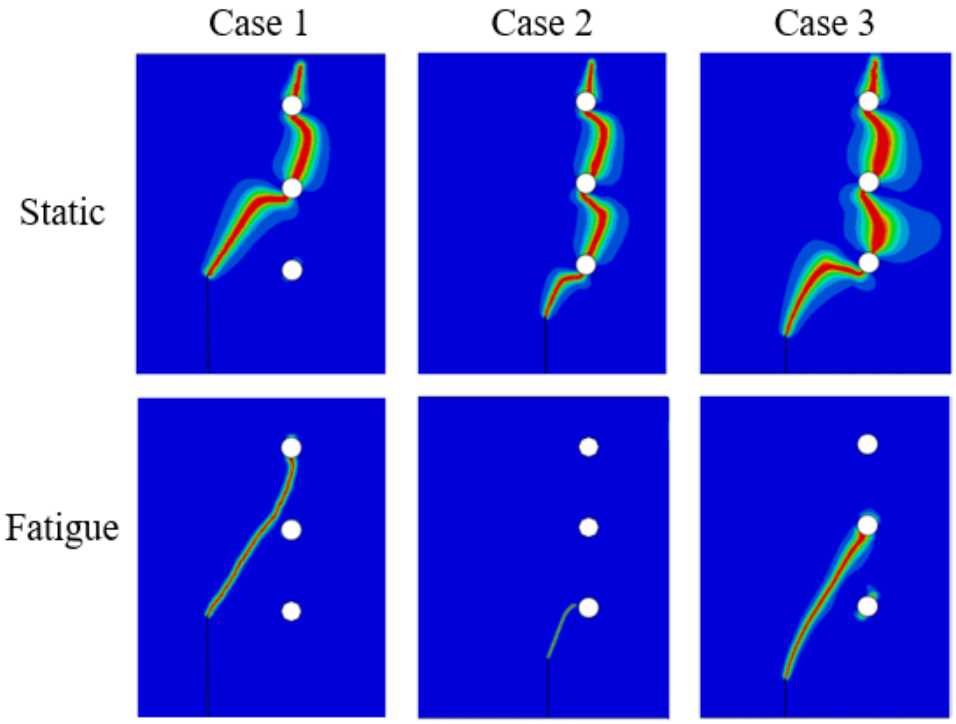

Figure 3.12: B-type static(up) and fatigue(down) crack path comparisons

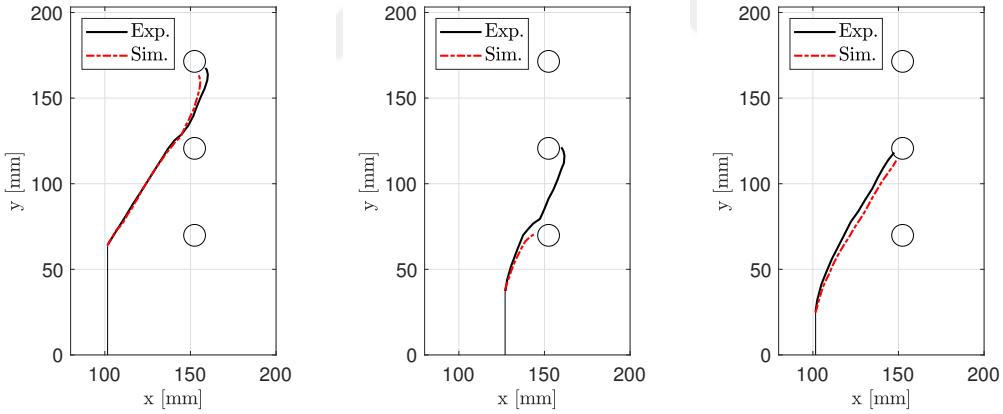

Figure 3.13: Crack path comparison between experimental and fatigue results

orders associated with fatigue failure. The only way then is to have a representative damage system where a single simulated cycle represents the fatigue damage caused by a set number of real cycles.

The lack of unconditional stability sets a minimum increment requirement during loading. However, in the case where the crack growth is spread over a large number

of cycles (10,000 perhaps), per cycle, the evolution of the phase field is minimal, allowing us to to treat each cycle comfortably as a linear problem, hence loosening the increment requirement significantly and buying a computational advantage. Therefore, simulating cycles in the order of 10^5 is not completely out of reach.

3.3 Simulating fatigue through a representative load and a zone-based retardation approach

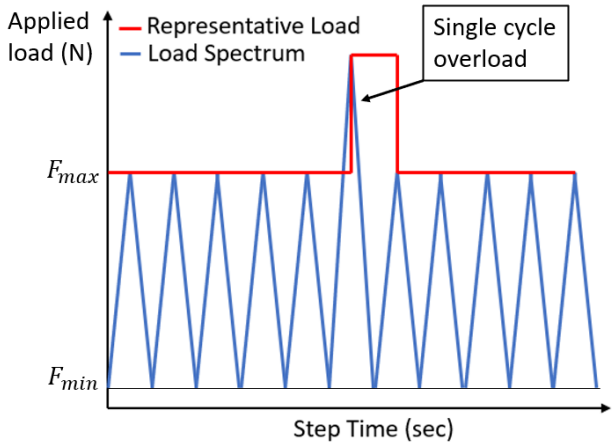

Figure 3.14: Representative load visualized

Models like [32] apply each individual load, accumulating damage to fatigue the material. This is computationally an almost impossible task, because the number of cycles that need to be applied to match experimental HCF data are in the order of 10^6. Some studies solve this through the application of a representative load, where the damage accumulated within a given unit of time represents a certain number of cycles (see [37]). This model applies a similar approach to applying fatigue loading conditions, as visualized in Figure 3.14. The maximum load is held constant, while the fracture toughness degrades over time, similar to creep boundary conditions. The fracture toughness degrades per time increment. Inspired partly by the work in [85] α:

$$\Delta\alpha = \begin{cases} \Delta t g((1-R)\psi_0 - \psi_{\text{th}}) & \text{if } \psi_0 - \psi_{\text{th}} \geq 0 \\ 0 & \text{otherwise} \end{cases} \tag{3.9}$$

where ψ_{th} is an energy threshold below which no fatigue damage is accumulated. In a physical sense, it may be interpreted as the endurance limit. The Δt term ensures that

the increment size does not seriously influence fatigue damage evolution. The applied load may be varied through changing the maximum load and R through different time frames. A linear relation between the total time taken for fracture and the total cycles required for fracture is established for calibration. Hence every second of time represents a certain number of applied cycles.

A crack retardation model is designed for this particular framework through the description of a region in which fatigue damage accumulation is reduced when an overload is applied. This region is described in energy terms by a limit H_{lim} where the region consists of the area where this energy density limit is exceeded upon the application of the overload. Higher overloads translate to a larger retardation region. The equations proposed for this model have been selected based on their influence on the crack evolution following an overload, through a system of trial and error.

The overload itself is characterized by the ratio between the energy densities of consecutive increments ψ_n/ψ_{n+1}. When this ratio significantly exceeds 1, an overload is said to have been applied. This ensures that the overload is characterized by a drop back to the regular load level, rather than the increase to the overload.

Upon application of the overload, the incremental fatigue damage within the retardation region is reduced through a retardation factor η. This factor is set to 0, and is proposed to evolve as follows during the overload increment:

$$\eta = C(1 - \frac{1.5}{1.5^{H/H_{\text{lim}}}}) \tag{3.10}$$

where C has been found to control the growth rate of the crack directly following the overload. An exponential relation is proposed as it ensures that retardation is highest at the crack tip and then gradually reduces to 0 at the border of the retardation zone defined by H_{lim}. This is preferred over a uniform value of η in the retardation zone, as when the crack reaches the zone border, nucleation can be triggered outside the zone, leading to uneven crack growth.

The distribution of η is set in the overload increment, implying that there is no further evolution during the rest of the crack life unless another overload is applied. C is proposed to have a direct dependency on the overload ratio and after trial and error, is described as thus:

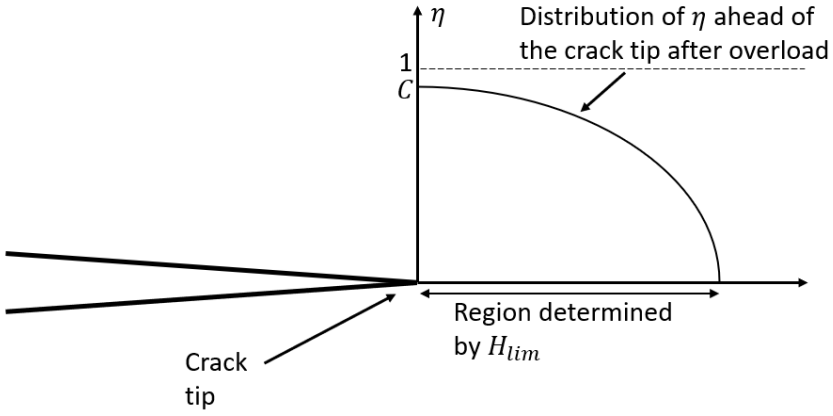

Figure 3.15: η distribution ahead of the crack tip following the overload

$$C = \arctan(a_1(\frac{\psi_n}{\psi_{n+1}} - 1)^{a_2})(\frac{2}{\pi}) \tag{3.11}$$

where a_1 and a_2 are parameters to be calibrated to the experimental overload results. The choice of this particular function fulfills several requirements. It establishes an asymptotic upper limit of 1 for η and when no overload is applied, $\eta = 0$. η is not allowed to reach a value of 1 to prevent crack arrest where no further fatigue damage accumulation occurs. C scales non-linearly, based on the severity of the overload. At higher overloads, this function translates to slower crack evolution at the crack tip. The value of C determines the slope of the crack evolution curve following the overload cycle, hence greatly influencing the gain in fatigue life following the overload cycle. Alternative descriptions of C with alternative features may also be considered.

The fatigue damage variable evolution may now be defined as thus:

$$\Delta\alpha = \begin{cases} \Delta t g((1-R)\psi_0 - \psi_{\text{th}}).(1-\eta) & \text{if } \psi_0 - \psi_{\text{th}} \geq 0 \\ 0 & \text{otherwise.} \end{cases} \tag{3.12}$$

The algorithm is visualized in Figure 3.16. In the following section, the capability of the described framework in simulating crack retardation under applied overloads is tested. A comparison with experimental results for crack evolution curves is made for two simulated specimens. Furthermore, the Type B 3-point bending test crack path studies are also simulated.

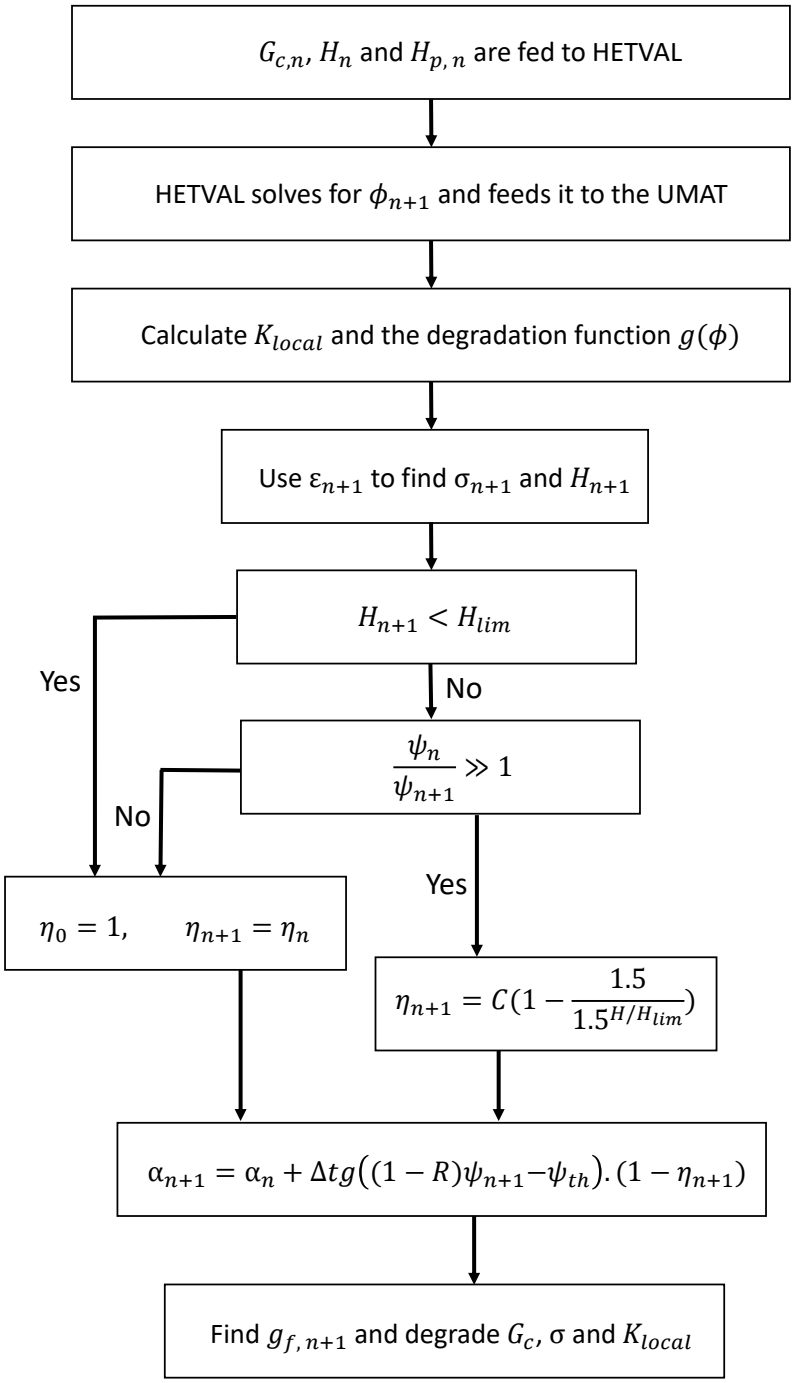

Figure 3.16: Representative load algorithm visualized

3.3.1 CT specimen

E (MPa)	Poisson's Ratio	Length Scale(mm)	H_{lim}(J)
194,000	0.3	0.5	0.55
G_{c} (N/mm)	α_{T}(J)	ψ_{th}(J)	
100	10	1	

Table 3.3: Material parameters for QSTE340TM steel

The CT specimen described in the previous chapter is once more simulated. The simulation parameters are described in Table 3.3. A fixed representative load is applied to the upper hole reference point, differing from the previous chapter. An increment size convergence study is performed to circumvent the unconditional stability of the staggered solution scheme as well as ensure that the increment size's influence on the fatigue damage variable remains minimal. Sufficient convergence is found at an increment size of 0.01 as shown in Figure 3.17, with negligible variation in the fatigue life at a smaller increment size.

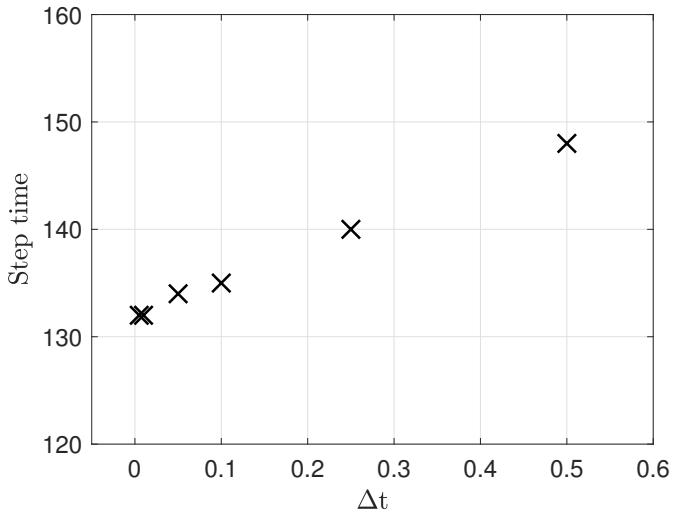

Figure 3.17: Time step convergence study results, step size vs. total step time required for 5 mm crack growth.

A comparison with the experimental results of [76] is made. The exponent n of the fatigue degradation function, Eq. 3.2 is taken as 3. The function for the retardation

factor η is calibrated to the experimental results for 1.5 and 2 times overload levels. The calibration is performed as follows. First H_{lim} is determined by matching the retardation zone size. This is found from a vs N curves by evaluating how far the crack grows before the original crack growth rate is recovered. A value of 0.55 MPa is found to be sufficient for H_{lim} considering the experimental evidence. Then, C values in Eq. 3.10 are found for each overload level by comparing the initial slope following the overload and matching the total life. Using these C values, a_1 and a_2 in Eq. 3.11 are calibrated. a_1 and a_2 are fit to values of 1.152 and 2.389, respectively, for the given experimental results. An additional result for 1.7 overload level is found to demonstrate the performance of the calibrated model.

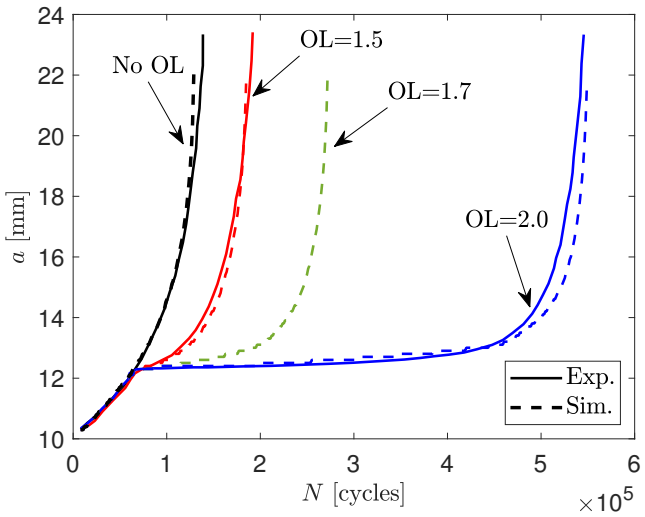

Figure 3.18: Comparison of experimental and phase field simulation results of crack length evolution for the CT specimen with single cycle overloads. Crack length, a, vs. total number of cycles N. Experiments are from [76].

The simulation results are plotted in Figures 3.18 and 3.19. The model is found capable of producing both the increase in fatigue life and crack evolution curves that match the experimental findings in [76]. Furthermore, experimental and numerical crack growth rate vs. stress intensity factor range results are shown in Figure 3.19. Crack growth rate is calculated from simulation results using $da/dN = \Delta a/\Delta N$ and ΔK is obtained following [76]. The simulation results correspond closely to the experimental trends without the overload. The model is able to capture Paris-Erdogan law, producing a linear relation between the logarithmic crack growth rate

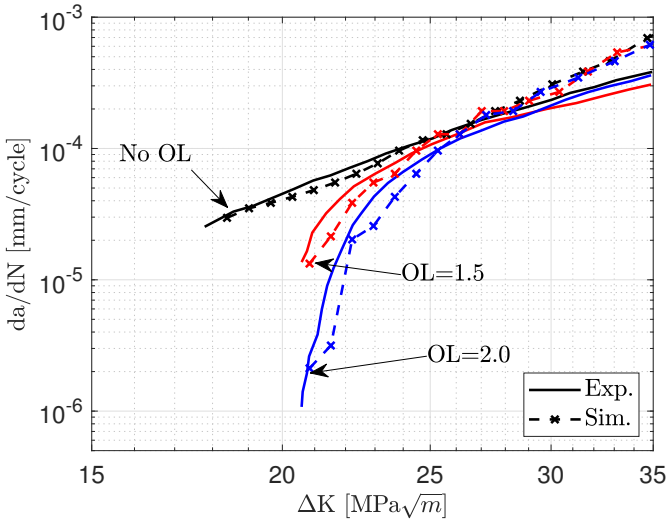

Figure 3.19: Comparison of experimental and phase field simulation results of crack length evolution for the CT specimen with single cycle overloads. da/dN vs. ΔK. Experiments are from [76].

and the logarithmic stress intensity factor range with the given parameter set. After a single cycle overload, the model is demonstrated to accurately capture the reduction in the crack growth rate. For both overload cases, the crack growth rate recovers to its original level after the crack has crossed the retardation region. It is observed that the model overestimates the growth rate at higher crack lengths. This may be due to crack growth occurring over a relatively small number of increments in that section of fatigue life leading to possible stability issues. Or it may be due to the choice of n, whose influence is demonstrated in the next section. From experimental crack growth rate vs. ΔK data, an initial estimate for the parameters of Eq. 3.10 can be obtained by using the ratio of crack growth rate before and after overload. Moreover, H_{lim} can be approximated through the range of crack length where the original crack growth rate recovers after the application of an overload.

The distribution of the retardation factor η following the overload describes both the retardation zone size and the intensity of the growth rate retardation. In Figure 3.20, the η distribution for 5 different load and overload cases is visualized. It is apparent that higher overload levels translate to a larger retardation zone as well as higher values for η, leading to significantly stronger gains in fatigue life. For larger applied

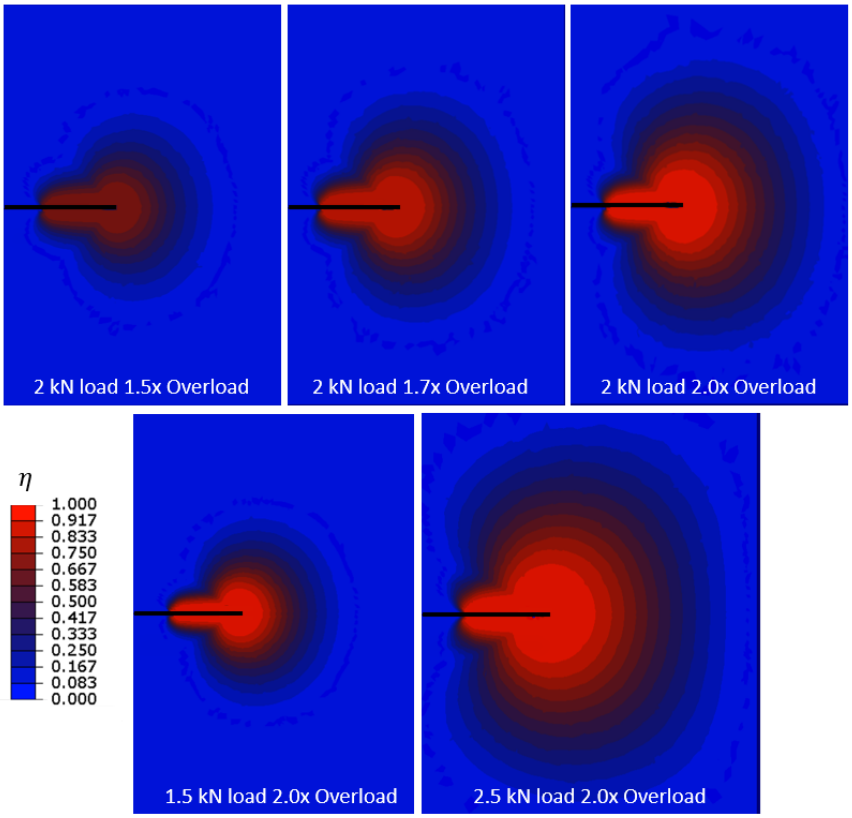

Figure 3.20: η distributions in the crack retardation zone for various overload levels.

loads, the retardation zone size is consequently larger having a direct dependence on the strain energy density around the crack tip. However, the maximum value of η remains the same. It should be noted that while the zone size is influenced by both the load level and the overload amount, in this model, the intensity of η is solely dependent on the overload ratio. A comparison with existing retardation models such as the Wheeler model [48], suggests that the retardation parameter should also have a load level dependence, establishing a closer correlation between the zone size and the retardation parameter.

The influence of the parameter H_{lim} which describes the size of the retardation zone is also demonstrated. Higher values of H_{lim} describe smaller zone sizes which are observed to translate to lower crack life gains when an overload is applied. This effect is far more noticeable at a higher overload. An interesting effect of lowering the zone size is that a sudden jump in the crack length is observed when the crack is exiting the zone. This is due to the distribution of η, whose function is tailored to

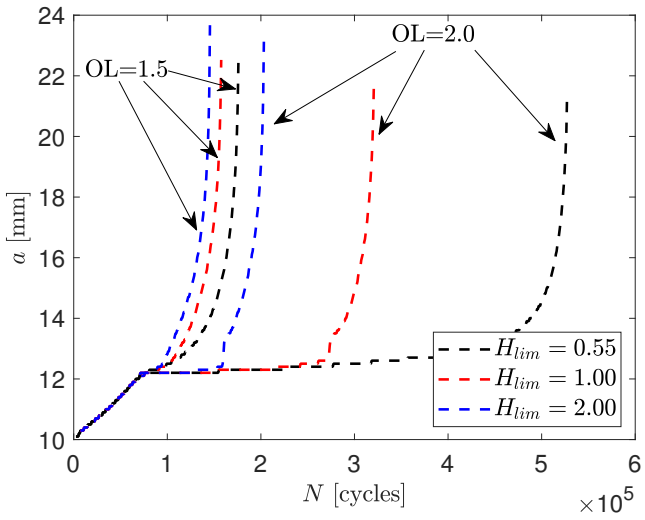

Figure 3.21: Influence of H_{lim} on overload crack life gains

suit H_{lim}. Eq. 3.10 must facilitate sufficient smoothness or damage accumulation at the outskirts of the retardation zone can lead to uneven crack evolution in that region. This implies that this function must be re-calibrated for larger values of H_{lim}. Later iterations of the model could eventually establish a closer relation between the zone size and the η distribution, eliminating the need for excessive calibration.

3.3.2 CCT specimen

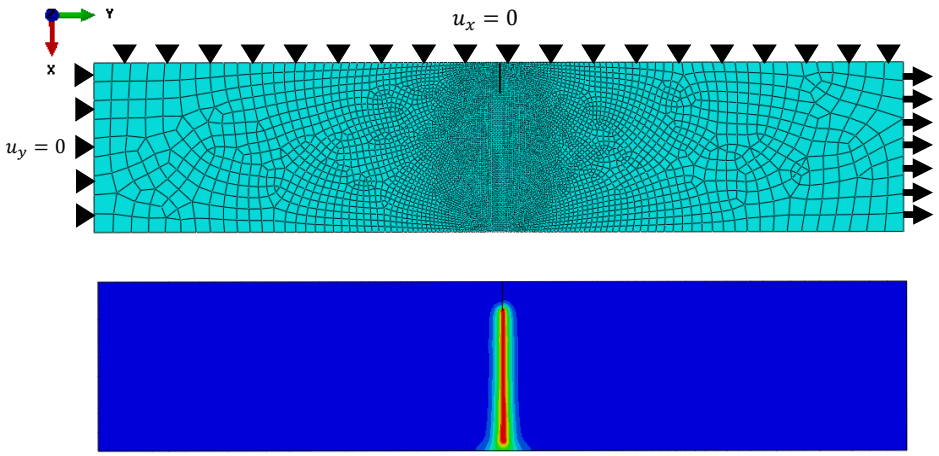

Figure 3.22: CCT symmetric model

This part covers the simulations results of the fatigue crack growth results with a single cycle overload applied at different intensities for a center-cracked tension panel (CCT) specimen. The simulation results are compared to the experimental data presented in [77]. The material properties of AM60B magnesium alloy are utilized as shown in Table 3.4. Half of the model is simulated through a symmetry boundary condition with a 3 mm geometric pre-crack as depicted in Figure 3.22. A constant load of 45 MPa is applied to the right face, while the opposite face's movement is restricted in the y-direction. Deformation in the x-direction is restricted for the symmetry face. Similar to the previous example, 2D plane stress elements (CPS4T) are utilized with a 0.15 mm minimum element size along the expected crack path.

E(MPa)	Poisson's Ratio	Length Scale(mm)	H_{lim}(J)
40,000	0.3	0.5	0.18
G_{c}(N/mm)	α_{T}(J)	ψ_{th}(J)	
70	3	0.2	

Table 3.4: Material parameters for AM60B magnesium

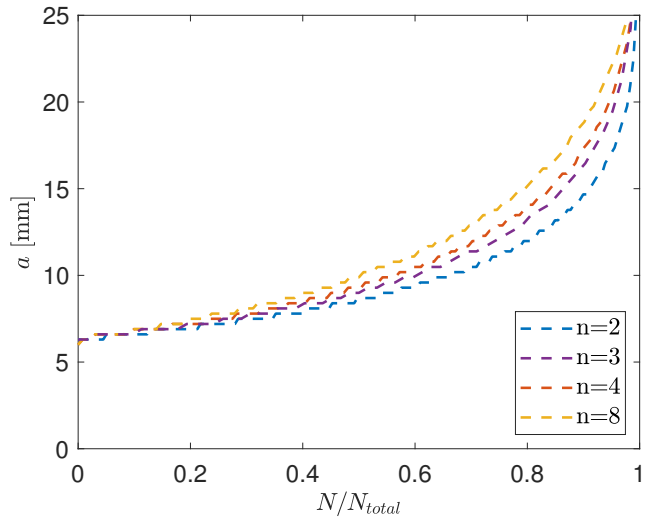

Figure 3.23: Effect of n on the crack growth rate. Crack length, a, vs. normalized cycles, N/N_{total}.

The influence of the exponent of the fatigue degradation function is explored with the CCT specimen as shown in Figures 3.23 and 3.24. The normalized crack evolution

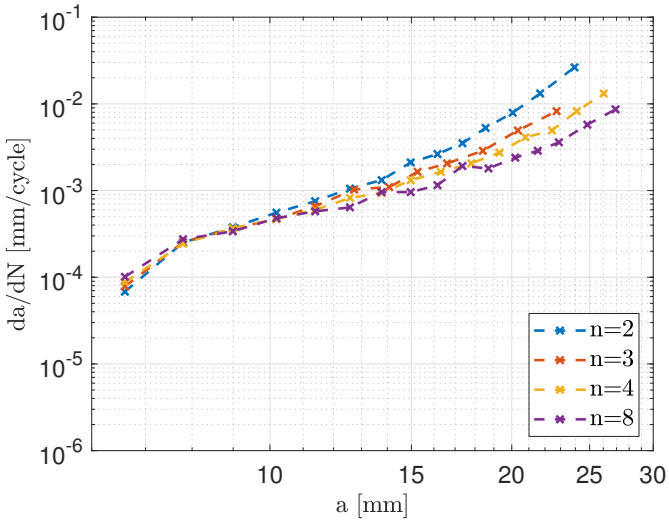

Figure 3.24: Effect of n on the crack growth rate. da/dN vs. ΔK

curve and the crack growth rate vs. crack length in a logarithmic scale are plotted for various values of the exponent n with the crack growth. For higher values of n, the crack growth is found to be faster during the earlier phase of life, while growing relatively slower during the later phase, leading to what may be described as less steep evolution curve. n seems to controls the slope of the Paris-Erdogan law behavior with higher values of n translating to a less steep slope. In this way n could be considered a material parameter for the current model.

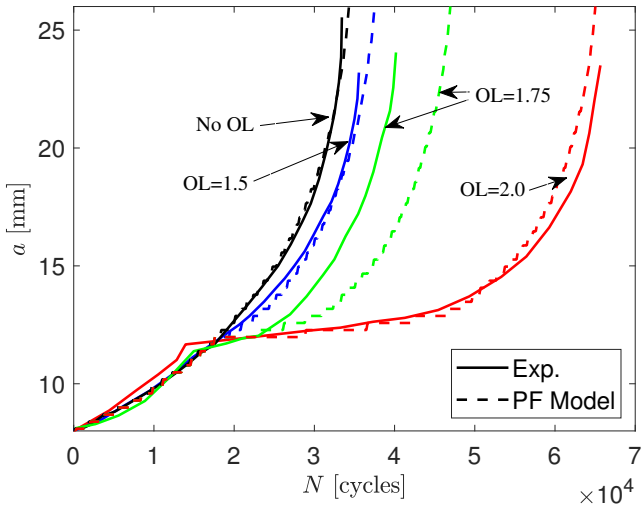

Figure 3.25: Crack evolution comparison for experimental and simulation results

Through calibration of both H_{lim} and η, the responses for different overload levels could be recreated. As in the previous section, an arc-tangent function is used to describe η, with calibration performed using the 1.5 and 2 times overload results. The performance of the function is then checked for 1.75 times overload. The results overestimate the life gain for 1.75 times the overload, implying that perhaps an arc-tangent function is not perfectly suited to describe the retardation coefficient's relationship with the overload level. Comparisons with further experimental data could facilitate better formulations to describe η, incorporating effects such as crack arrest.

3.3.3 Three point notched bending test with asymmetric perforations

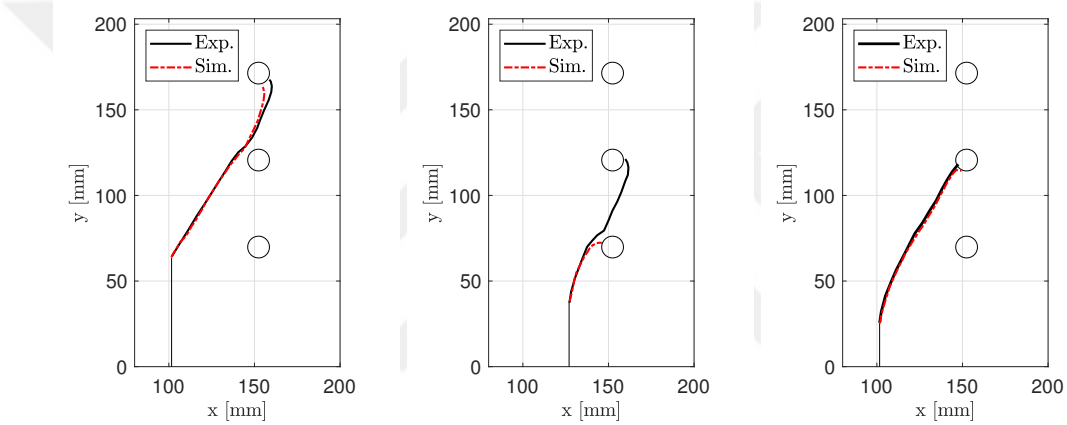

Figure 3.26: Crack path comparison between experimental and fatigue results

Following on the model from the previous section, fatigue simulations are conducted for the notched bending test with a fixed displacement applied symmetrically at the top hole reference point. The results are visualized in Figure 3.26. It can be observed that this model is also capable of capturing the crack paths with great accuracy, with Case 2B being the notable exception once more. In fact for Case 3B, the result with the representative load model seems more accurate when a comparison is drawn with the crack closure model. With only slight variation, the close correspondence between the crack path results for both models is an expected result, as while the fatigue damage accumulation mechanisms differ, the driving force remains the strain energy density, with the crack growing in a direction where this term is maximum.

CHAPTER 4

PHASE FIELD MODELING OF DUCTILE FRACTURE THROUGH THE MMC MODEL

This chapter pertains to the extension of the brittle phase field model to a ductile setting, where a non-linear J2 plasticity model is coupled with the phase field paradigm. The theory behind the extension to ductility involves the introduction of a plastic component to the crack driving force. The extension of the brittle paradigm to a ductile phase field framework has been done in a number of ways in the literature. The coupling mechanism between the phase field and the evolution of plasticity is the defining feature of such models.

Duda et al. [86] opts to not couple the plastic damage, leading to a model described as brittle fracture in an elasto-plastic solid, with limited plastic deformation at the crack tip before failure. Ambati et al. [87] couples their model by introducing a coupling term that acts through the degradation function. Borden et al. [62] couples the model by introducing a plastic component to the crack driving force and degrading it as the phase field evolves. In an approach mimicking some phase field fatigue frameworks, Yin et al. [88] introduces a model that degrades the fracture toughness through the accumulating plastic strain, ensuring that the crack driving force remains elastic. Dittman et al. [89] simulate a porous ductile phase field model where the plastic contribution to the crack driving force is driven by the Gurson–Tvergaard–Needleman (GTN) model. The ductile phase field framework has also been adapted to fracture in shell structures (see [90]).

In this study, the coupling is performed through the introduction of a plastic degradation function to the plastic component of the crack driving force. The evolution of plastic damage is controlled through the introduction of a threshold. Both plastic

strain thresholds (see [91]) and energy thresholds (see [62]) have been employed in the literature. This study employs the latter. The Modified Mohr Coulomb (MMC) model [58] is integrated in the framework through scaling the plastic damage evolution. The model performance is gauged through various benchmark specimen simulations by attempting to match the experimental load-displacement curves from [92] and [93] while using their respective material and damage parameters. The Nakajima test is also simulated for specimens of varying width and the crack paths and major-minor strain evolution curve are visualized.

4.1 Extension to Plasticity

The incorporation of plasticity in the brittle framework is facilitated through the introduction of an additional plastic energy term to the total energy functional,

$$E = E_{\mathrm{s}} + E_{\mathrm{e}} + E_{\mathrm{p}} \tag{4.1}$$

where E_{p} is defined as thus:

$$E_{\mathrm{p}} = g_{\mathrm{p}}(\phi) W_{\mathrm{p}}(\boldsymbol{\varepsilon}_{\mathrm{p}}) \tag{4.2}$$

where g_p is the plastic degradation function, taken identical to the elastic degradation function in the context of this thesis for computational simplicity. The degradation function has great control over the evolution of the flow stress. It is important to choose a function that prevents premature degradation, to ensure that existing hardening rules can be efficiently coupled with the phase field paradigm without understating the flow curve. To this end, the following degradation function [65] is chosen:

$$g = \frac{(1-\phi)^2}{(k-(k-1)(1-\phi)^2)} + k \tag{4.3}$$

where, k is taken as 0.01, a far larger constant in comparison to the fatigue case. This is because far larger deformations are involved, leading to mesh distortion and hence convergence issues, necessitating that the mesh be allowed to retain some structural integrity even at complete failure. W_{p} is taken as a scaled version of the plastic dissipation and its evolution is described as thus:

$$\dot{W}_{\mathrm{p}} = \frac{\sigma_{\mathrm{flow}} \dot{\varepsilon}^{\mathrm{p}}_{\mathrm{eq}}}{\varepsilon_{\mathrm{f}}} \tag{4.4}$$

where ε_{f} is introduced as a scaling parameter of sorts which controls the evolution of plastic damage according to the stress state. It is retrieved from the MMC model as follows:

$$\varepsilon_f = \left\{ \frac{K}{\hat{C}_2} \left[\hat{C}_3 + \frac{\sqrt{3}}{2-\sqrt{3}} \left(\hat{C}_4^* - \hat{C}_3 \right) \left(\sec\left(\frac{-L\pi}{6} \right) - 1 \right) \right] \times \left[\sqrt{\frac{1+\hat{C}_1^2}{3}} \cos\left(\frac{-L\pi}{6} \right) + \hat{C}_1 \left(T + \frac{1}{3} \sin\left(\frac{-L\pi}{6} \right) \right) \right] \right\}^{-1/n} \tag{4.5}$$

$$\hat{C}_4^* = \begin{cases} 1 & -1 \leq L \leq 0 \\ \hat{C}_4 & 0 < L \leq 1 \end{cases} \tag{4.6}$$

where T and L are the stress triaxiality and Lode parameter respectively, calculated as follows:

$$T = \frac{\sigma_{\mathrm{h}}}{\sigma_{\mathrm{eq}}} \tag{4.7}$$

$$L = \frac{2\sigma_1 - \sigma_2 - \sigma_3}{\sigma_1 - \sigma_3} \tag{4.8}$$

where σ_1, σ_2 and σ_3 are principal stresses and σ_{h} and σ_{eq} are the hydrostatic and von Mises stresses respectively, found as follows:

$$\sigma_{\mathrm{h}} = \frac{\sigma_{11} + \sigma_{22} + \sigma_{33}}{3} \tag{4.9}$$

$$\sigma_{\mathrm{eq}} = \sqrt{\frac{(\sigma_{11}-\sigma_{22})^2 + (\sigma_{22}-\sigma_{33})^2 + (\sigma_{11}-\sigma_{33})^2 + 6(\sigma_{12}^2 + \sigma_{23}^2 + \sigma_{31}^2)}{2}} \tag{4.10}$$

The classical application of the MMC model is done through a damage variable defined as thus:

$$D = \int \frac{\dot{\varepsilon}_{\mathrm{eq}}^{\mathrm{p}}}{\varepsilon_{\mathrm{f}}} dt \tag{4.11}$$

where the material is considered to have completely failed when the value of D has reached 1. A further computational measure is necessitated by the nature of ductile phase field models. Ductile materials feature fracture toughness values that are several scales higher than those for brittle materials. Furthermore, the evolution of plastic damage is relatively slower than elastic damage would be at similar strains. This leads us to slow evolution of the phase field where the stress peaks early and then gradually degrades over a large amount of strain; a completely unrealistic material response. This is solved through the introduction of a plastic damage threshold. Both plastic strain thresholds (e.g. [91]) and energy thresholds (e.g. [62]) have been

employed in literature. An energy threshold is utilized in this study, by replacing W_p with the following:

$$\langle W_{\mathrm{p}} - W_{\mathrm{p}}^{\mathrm{c}} \rangle. \tag{4.12}$$

Plastic damage hence does not evolve until a certain critical threshold is exceeded. This significantly change the role of existing parameters, where G_{c} no longer controls the fracture toughness, with this role passing to $W_{\mathrm{p}}^{\mathrm{c}}$. Instead, it controls the rate at which degradation happens after failure. The length scale is also demoted to a similar role. The strong form may be described as follows:

$$G_{\mathrm{c}}(\frac{\phi}{l_0} - l_0 \nabla^2 \phi) \ - 2(1-\phi)(H + \langle W_{\mathrm{p}} - W_{\mathrm{p}}^{\mathrm{c}} \rangle) = 0. \tag{4.13}$$

An extended Voce hardening rule is utilized to describe the isotropic hardening of the material,

$$\sigma_{\mathrm{y}} = \sigma_0 + \sum_{i=1}^{3} Q_i (1 - \exp(-C_i \varepsilon_{\mathrm{eq}}^{\mathrm{p}})). \tag{4.14}$$

4.2 6016-T4 Aluminum Alloy Study

Several benchmark specimens are simulated with the ductile phase field model to observe its ability to capture both the crack path and the material response. 4 specimen geometries, namely notched tension (NT3, NT10), plane strain tension (PST) and in plane shear (ISS), are solved using the proposed phase field formulation for 6016-T4 aluminum alloy. The material, phase field and MMC properties (retrieved from [92]) are recorded in Tables 4.1, 4.2 and 4.3.

E(MPa)	ν	l_0(mm)	G_{c}(N/mm)	$W_{\mathrm{p}}^{\mathrm{c}}$(N.mm)
70000	0.3	1	50	275

Table 4.1: Elastic and phase field parameters

All simulations are performed with the implicit finite element solver Abaqus. Models are meshed with a fully integrated 3D (hexahedral) temperature-displacement coupled element (C3D8T in Abaqus) as shown in Fig 4.1. The average element size in the gauge section is 0.05 mm with 5 elements in the thickness direction in all FE models.

σ_0(MPa)	Q_1	C_1	Q_2	C_2	Q_3	C_3
135	19.04	87.05	142.22	10.06	75	3.08

Table 4.2: Voce hardening parameters

K	$\hat{C}_1$	$\hat{C}_2$	$\hat{C}_3$	$\hat{C}_4$	n
0.9969	0.01	0.5075	0.8820	1.0056	0.01122

Table 4.3: MMC damage parameters

Solutions are performed using automatic step size control with a maximum step size of 0.001 s and a total time of 1 s which is found to be an efficient value in terms of solution time and convergence. NT3, NT10 and ISS are pulled from the center of the top pin and held from the center of the bottom pin while allowing for rotation around the pins. Pin centers are connected to the specimen with the MPC beam constraint. For the PST specimen, the clamped regions are assumed to be rigid and modeled as rigid bodies in FE as shown in Fig. 1. The PST specimen is pulled upwards from the top rigid section and held fixed from the bottom rigid section. Only the middle portion of the ISS specimen is modeled for FE simulations to save computational time. In order to apply boundary conditions, top and bottom pin centers are connected to the FE mesh with the MPC beam constraint as shown in Figure 4.1 with black lines.

$W_{\mathrm{p}}^{\mathrm{c}}$ is calibrated to the material response, to achieve complete failure at the appropriate displacement and match experimental data. The influence of the threshold can be better visualized in Figure 4.2 where, in the absence of the a threshold, the load carrying capacity of the material reduces very gradually once the critical strain point has been reached. The addition of the threshold solves this problem and simulates a more immediate loss of structural integrity which is realistic. G_{c} is altered in order to control the stress drop at the point of total failure. This value is kept low, but not low enough to cause convergence issues or inflate the contribution of elasticity to the total damage. The load-displacement responses and crack patterns are visualized in Figures 4.3, 4.4, 4.5 and 4.6.

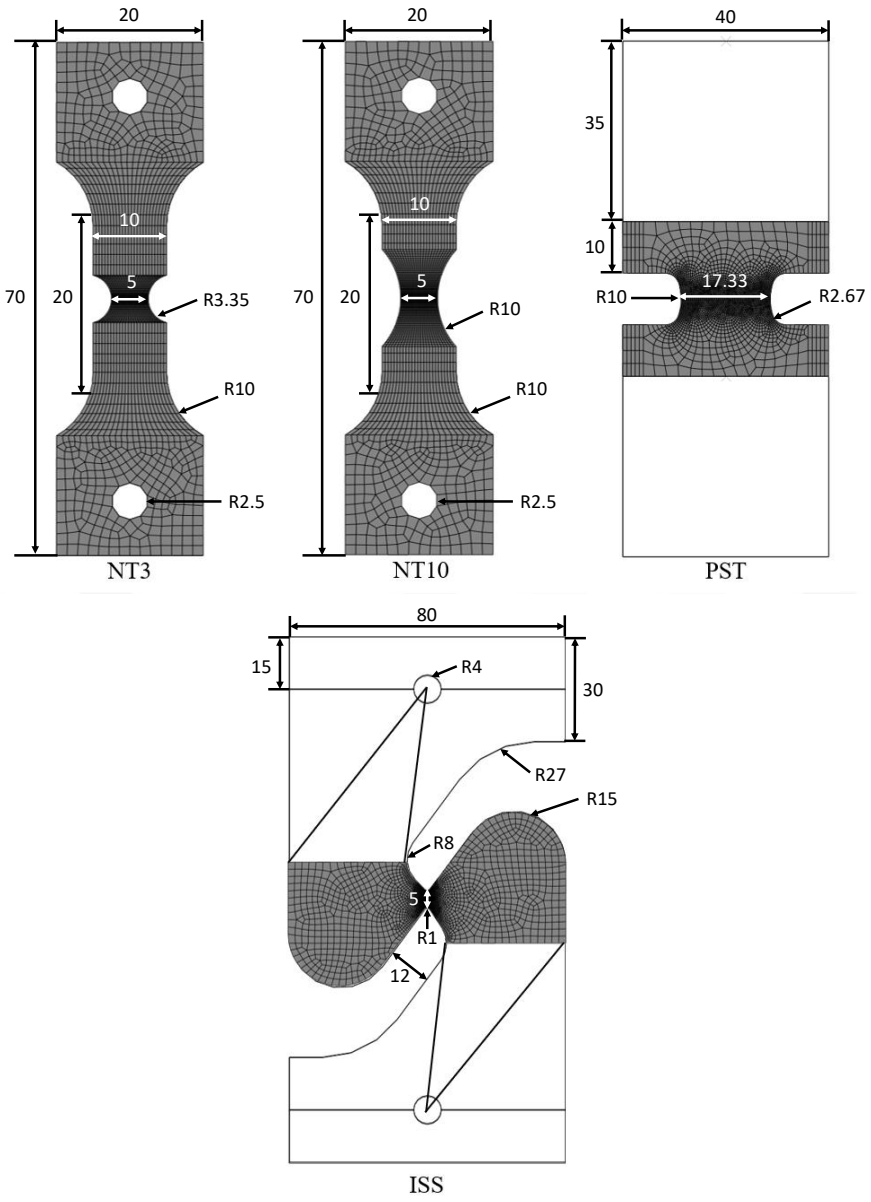

Figure 4.1: Mesh and dimensions for ductile specimens (mm)

It is found that the MMC based model is able to capture the material responses for various specimens with great accuracy. The only notable exception seems to be the ISS specimen. However, this is a feature of the MMC fit (see [92]), with the phase field MMC model reproducing the material response with a great deal of accuracy. The role of the plastic energy threshold is explored as shown in Figure 4.7. As expected, $W_{\mathrm{p}}^{\mathrm{c}}$ now controls the fracture toughness of the material, with fracture occurring at lower strains for lower $W_{\mathrm{p}}^{\mathrm{c}}$ values.

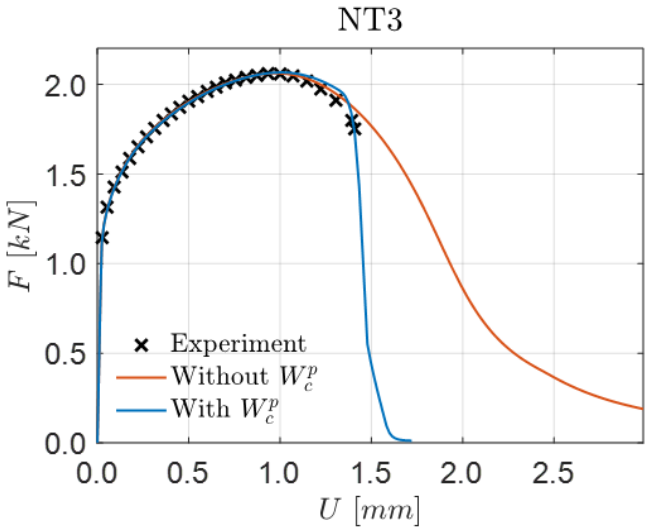

Figure 4.2: The effect of the threshold $W_{\mathrm{p}}^{\mathrm{c}}$ on the load displacement behavior

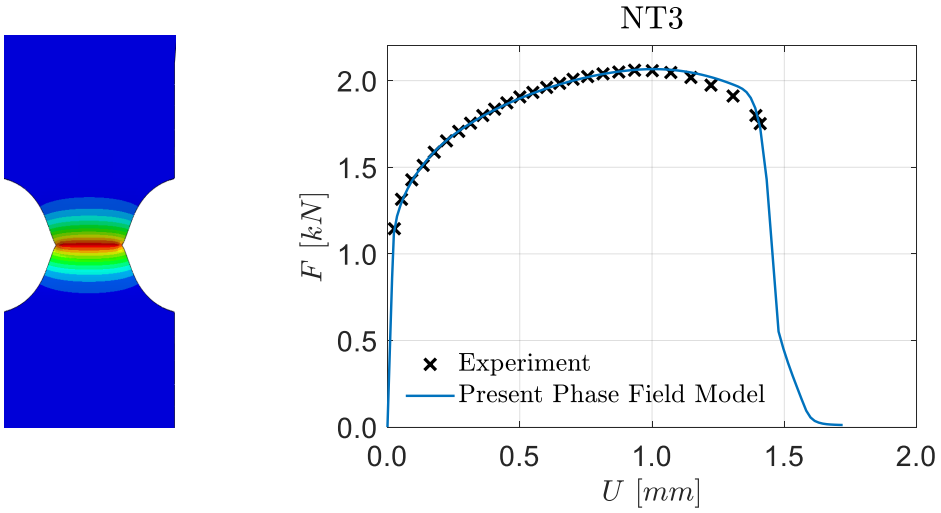

Figure 4.3: Phase Field and Load Displacement curve for NT3 specimen

The effect of varying length scale is also demonstrated with the results visualized in Figure 4.8. It is found that the diffuseness of the crack reduces at lower length scales as expected but the material response shows very light variation. This result may be treated as a good argument in favor of using a damage threshold. The length scale has been demonstrated to influence the fracture toughness, implying that a characteristic fracture toughness is difficult to establish for a material, requiring re-calibration at

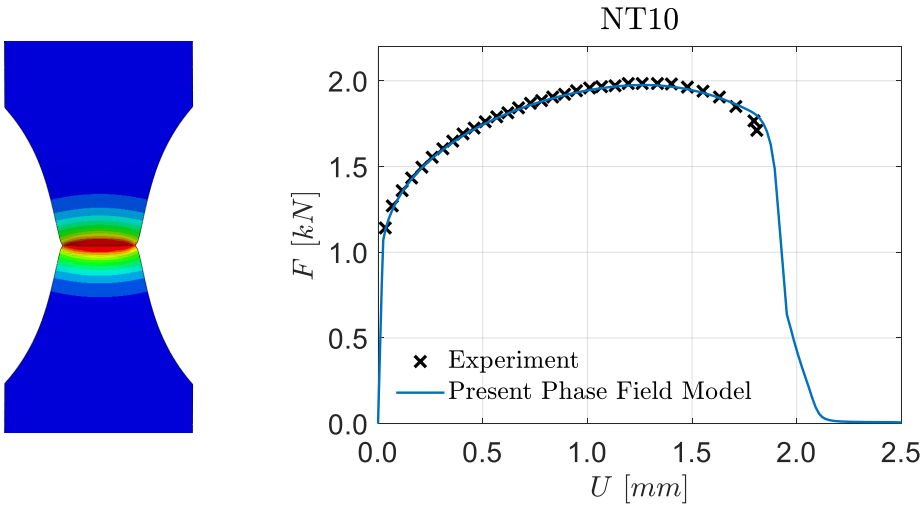

Figure 4.4: Phase Field and Load Displacement curve for NT10 specimen

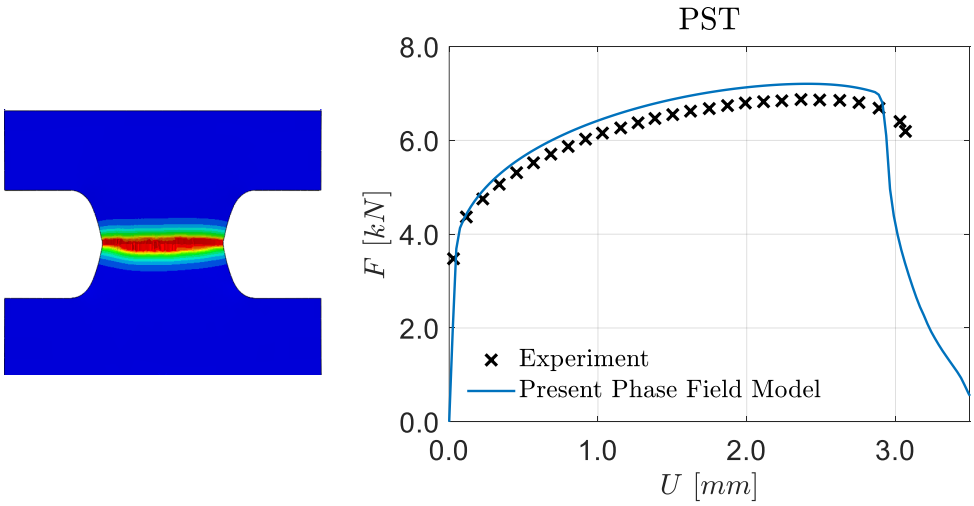

Figure 4.5: Phase Field and Load Displacement curve for PST specimen

problems of various scales. However, the threshold eliminates this influence, thereby allowing the damage threshold $W_{\mathrm{p}}^{\mathrm{c}}$ to be associated with a material in problems of any scale.

While the phase field fracture framework performs very well in brittle and fatigue

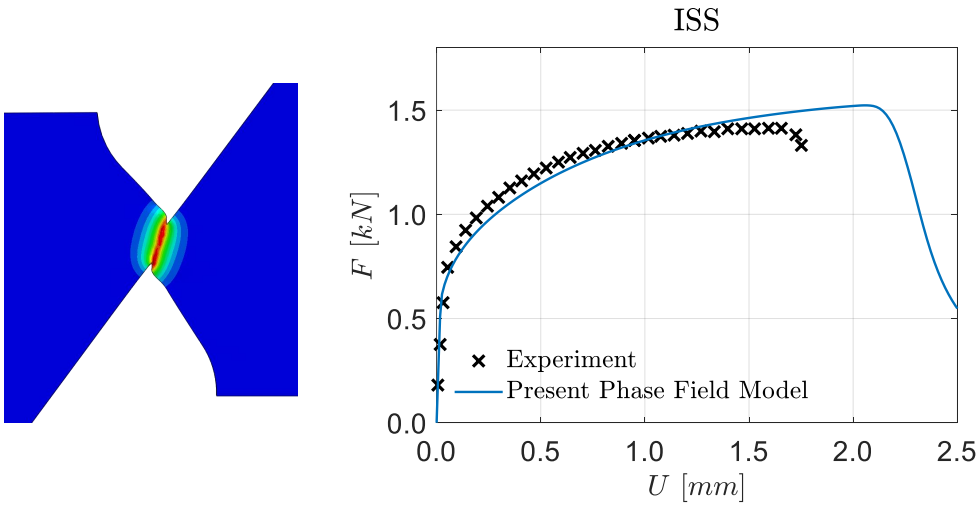

Figure 4.6: Phase Field and Load Displacement curve for ISS specimen

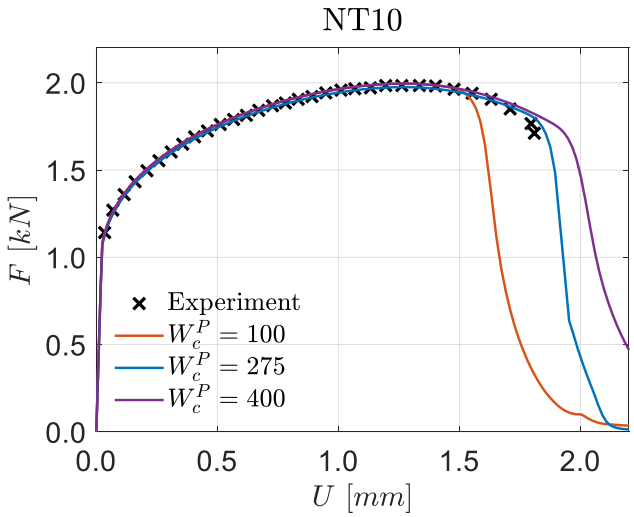

Figure 4.7: Load Displacement curves for different threshold values

conditions, its functionality as a damage model for ductile materials should be closely scrutinized. Rather than crack propagation, crack nucleation tends to be a more critical phenomenon in the applications of ductile fracture models. In this context, the phase field parameter can not be treated as a damage variable, as it only evolves rapidly at the point of fracture. Hence it can not be used to track how close to fracture our material is. That role can be better served by W_{p} where it may be compared to

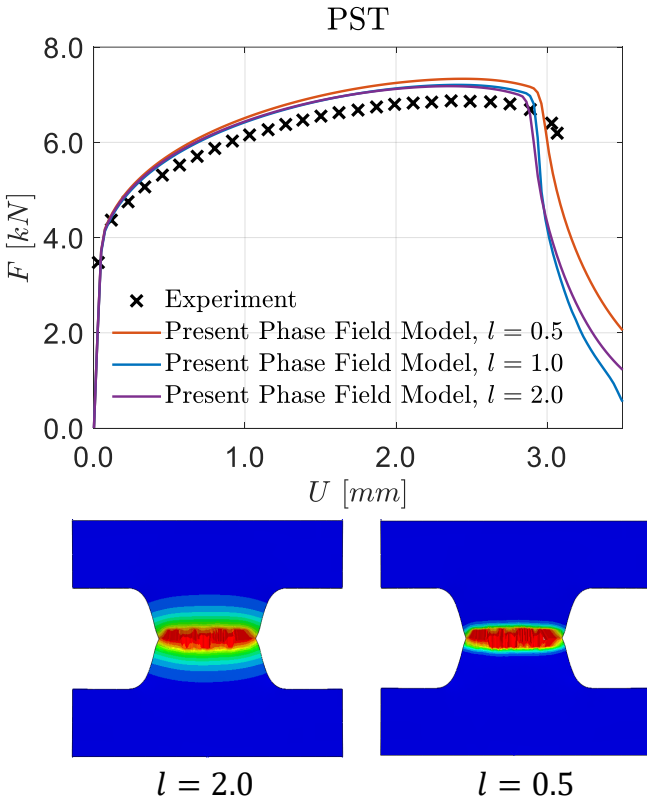

Figure 4.8: Load Displacement curves for different length scales

$W_{\mathrm{p}}^{\mathrm{c}}$ to get a sense of how close to fracture the material is.

4.3 Inconel 718 study

An additional study is performed to assess the utility of incorporating the MMC model in a ductile phase field framework. Benchmark specimens are simulated to observe gage the model's performance both with and without the . With the dimensions and boundary conditions taken from [93], 4 specimen geometries, namely smooth tension (ST), notched tension (NT), plane strain tension (PST) and in plane shear (ISS), are solved using the proposed phase field formulation for Inconel 718. Quarter models are simulated for the ST, NT and PST specimens for faster simulation time, with displacement in the x direction restricted on the y-z symmetry plane and displacement in the z direction restricted on the x-y symmetry plane. The element size is 0.1mm in the gauge section. The material, phase field and MMC properties (retrieved

from [93]) are recorded in Tables 4.4, 4.5 and 4.6.

The Voce hardening rule used in this section is altered to match the one in [93]. It is given as thus:

$$\sigma_{\mathrm{y}} = \sigma_0 + \sum_{i=1}^{2} q_i(1 - c_i \exp(-b_i \varepsilon_{\mathrm{eq}}^{\mathrm{p}})). \tag{4.15}$$

The MMC model is also altered to match the one in [93] to allow the use of their calibration parameters, where the Lode Parameter L is replace by the negative Lode angle parameter $-\bar{\theta}$. It may be calculated as follows:

$$\bar{\theta} = 1 - \frac{6\theta_L}{\pi}. \tag{4.16}$$

$$\cos(3\theta_L) = \frac{J_3}{2}\left(\frac{3}{J_2}\right)^{\frac{3}{2}} \tag{4.17}$$

where J_2 and J_3 are the second and third deviatoric stress invariants.

E(MPa)	ν	l_0(mm)	G_{c}(N/mm)	$W_{\mathrm{p}}^{\mathrm{c}}$(N.mm)
200000	0.294	1	70	1000

Table 4.4: Elastic and phase field parameters

σ_0(MPa)	q_1	q_2	b_1	b_2	c_1	c_2
789	499.6	499.6	106.7	4.351	0.1731	1.761

Table 4.5: Voce hardening parameters

K	$\hat{C}_1$	$\hat{C}_2$	$\hat{C}_3$	$\hat{C}_4$	n
1946	10.39	14420	4.517	1.0	2.216

Table 4.6: MMC damage parameters

The utility of adding the MMC model to a ductile phase field model is arguable. The addition of the MMC model allows far more precise calibration whereas without it, the only calibration parameter is $W_{\mathrm{p}}^{\mathrm{c}}$ which would alter the material response for the other specimens if calibration was attempted for this specimen. With the MMC parameters, however, calibration may be performed for all the specimens. Hence this is the advantage of incorporating the MMC model into a ductile phase field model.

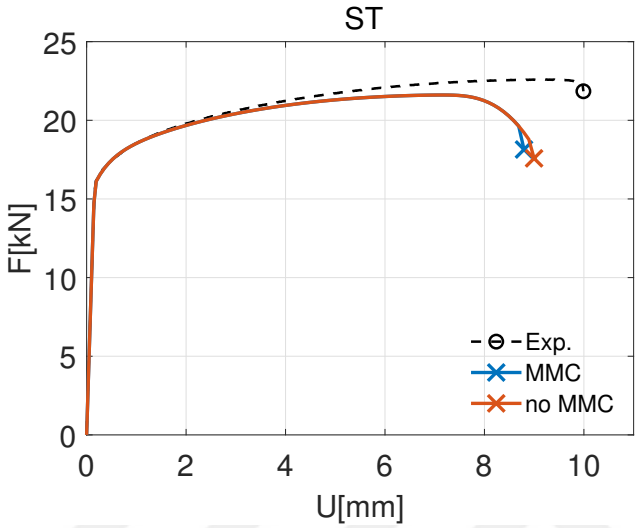

Figure 4.9: Phase Field and Load Displacement curves for ST specimen

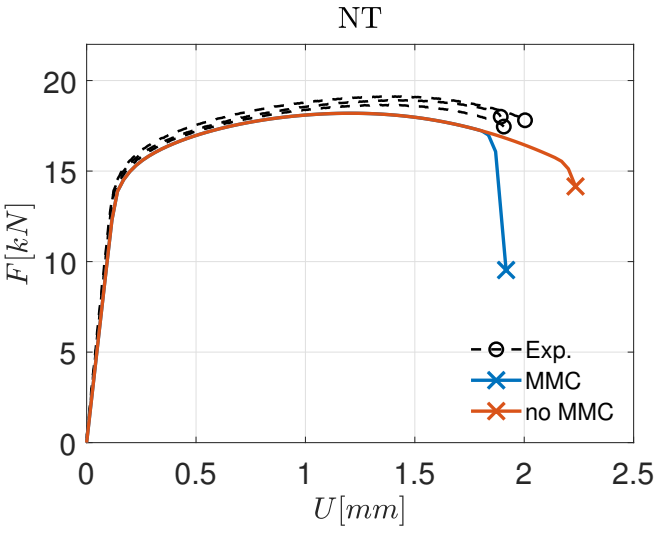

Figure 4.10: Phase Field and Load Displacement curves for NT specimen

To demonstrate the influence of incorporating the MMC model, the specimens are first solved without the scaling parameter sourced from the MMC equation, hence ε_{f}

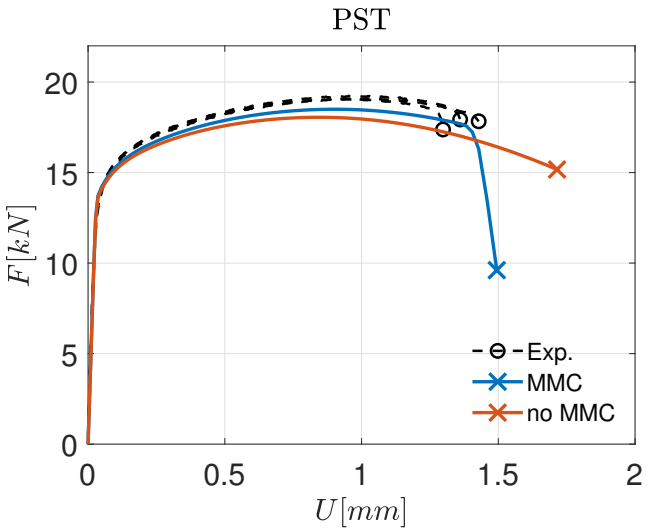

Figure 4.11: Phase Field and Load Displacement curves for PST specimen while varying G_c for the MMC and no MMC curves

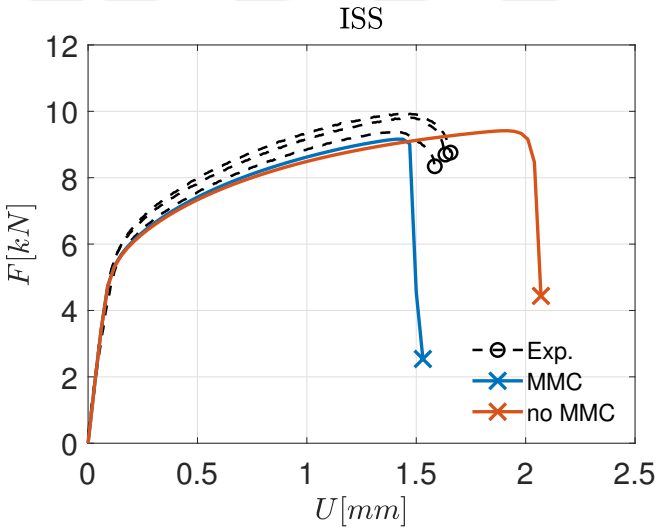

Figure 4.12: Phase Field and Load Displacement curves for ISS specimen while varying G_c for the MMC and no MMC curves

is fixed as 1. The threshold W_p^c is then calibrated using the mechanical response for the ST specimen. A value of 1000 N.mm is considered to sufficiently calibrate the response. The remaining three specimens are then simulated while employing this threshold. Following this, the MMC inclusive response is simulated, which requires re-calibration of the threshold as the MMC contribution ε_f scales the damage. Once more, the ST specimen is used to perform the calibration, with a value of 1250 N.mm

found to capture the material response with sufficient accuracy. The results are visualized in Figures 4.9, 4.10, 4.11 and 4.12. The specimens and crack development are visualized in Figure 4.13.

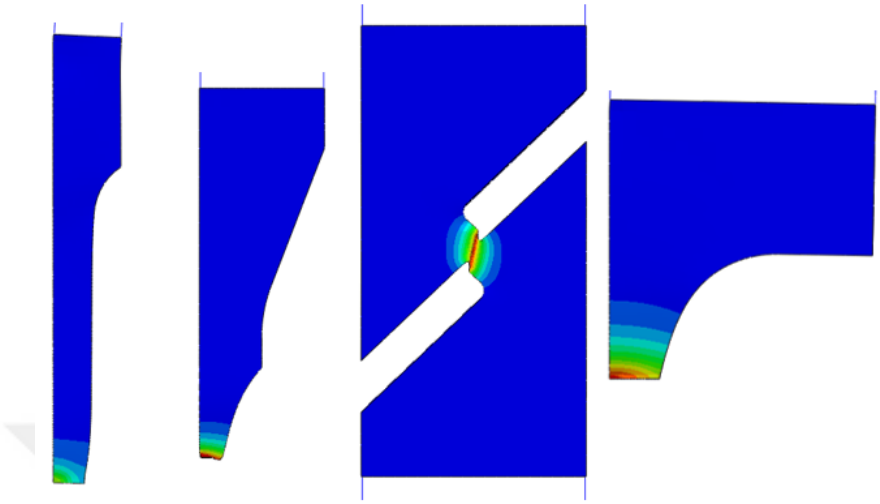

Figure 4.13: Specimens and crack evolution

When $W_{\mathrm{p}}^{\mathrm{c}}$ is calibrated for the ST specimen in the case without the MMC model, it directly leads to an overestimation in the failure strain for the other three specimens. This behavior is noted in [93] to be similar to the Cockcroft-Latham damage model [94] which is also calibrated through a single parameter. The MMC model however, successfully reproduces the material response for the following three specimens while employing only the ST specimen for calibrating $W_{\mathrm{p}}^{\mathrm{c}}$. Hence the compatibility of the MMC model with the phase field framework is once more demonstrated.

The simulation results are observed to be understated slightly, compared to the experimental curves. This may possibly be attributed to premature degradation associated with the elastic contribution to the crack driving force. A better choice of degradation function could improve this response. For the ISS and PST specimens, a slight disparity between the flow curves for the MMC and non-MMC results may be observed. This is because G_{c} is inflated (from 70 to 100) for the MMC results for these two specimens, to confirm whether the elastic contribution to the crack driving force is responsible for the premature degradation. At a higher value of G_{c}, the flow curve is less degraded, as the elastic contribution is now relatively smaller in comparison to G_{c}.

4.4 Nakazima test simulations

The Nakazima test was developed to determine the formability of materials for deep drawing operations. It involves several sheet metal specimens restrained by a die and deformed through a punch. The punch is pushed vertically until the specimen experiences crack initiation and subsequent crack growth. Both the punch and the die are taken as rigid bodies and the test sample is meshed with fully integrated 3D (hexahedral) temperature-displacement coupled elements. Frictionless contact is assumed between all interacting surfaces.

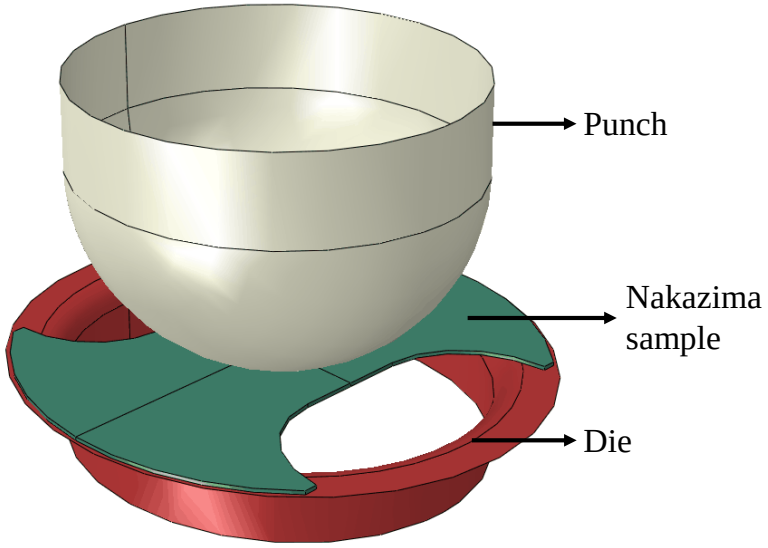

Figure 4.14: Simulation set up for the Nakazima test

The punch is modeled as a cylindrical surface transitioning into a hemispherical cap. The diameter is taken as 101.6 mm. The die and specimen dimensions are described in Figure 4.15. Specimen thickness is taken as 1 mm.

The Nakajima test demonstrates the phase field framework's ability to capture slanted crack paths, as demonstrated by the first two specimens. For these narrow specimens, the crack initiates horizontally at the center followed by slanted crack growth which is a pattern that can be observed experimentally [95, 96]. Horizontal crack development is obtained for wider specimens in agreement with the experimental observations. As for the radially symmetric specimen ($w = 175$) a cross crack pattern nucleates whose

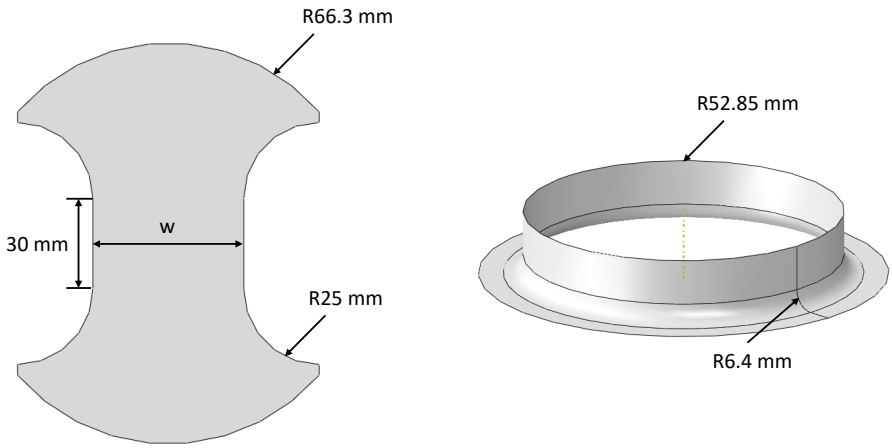

Figure 4.15: Specimen and die dimensions

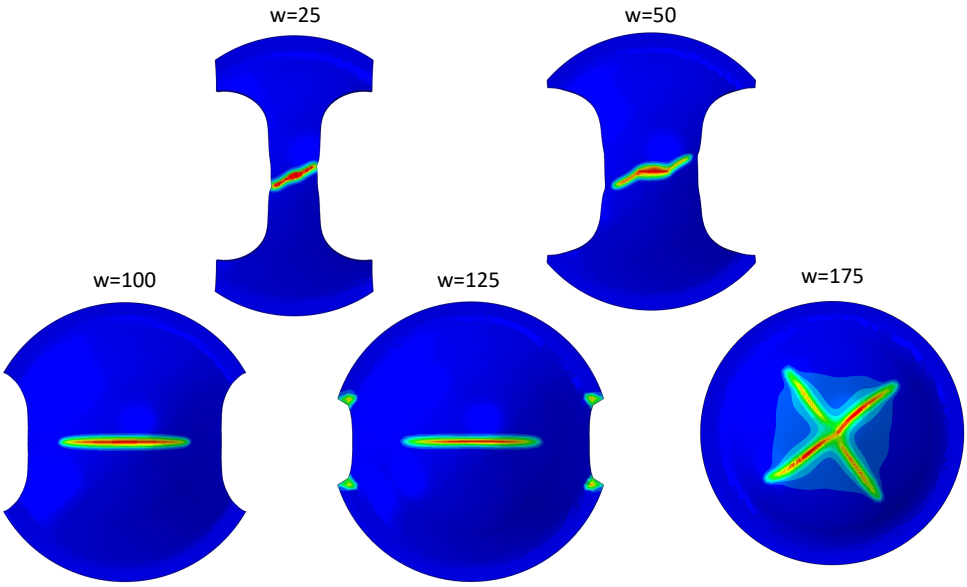

Figure 4.16: Crack paths for Nakazima specimens

orientation is most likely controlled by the mesh refinement employed. All cracks initiate at the outer surface rather than the surface in contact with the punch. For the case where $w = 125$, it can be observed that some damage plastic damage accumulates at the corners of the rim where deformation is not restricted. This is a phenomenon solely restricted to this case, occurring possibly due to stress concentrations caused by an insufficiently fine mesh in that region and is not found to distort the final result.

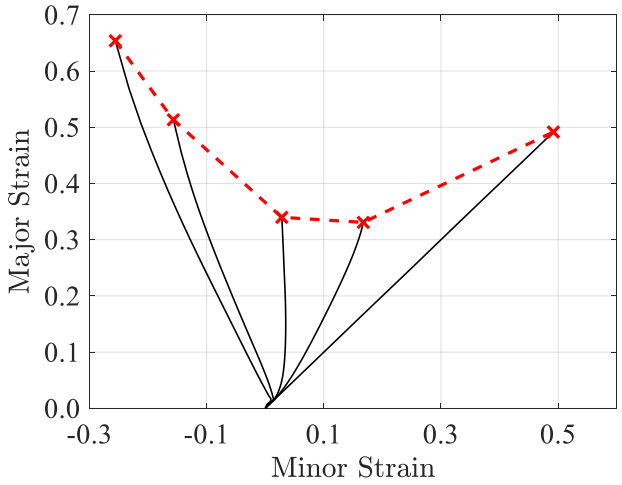

Figure 4.17: Fracture locus at major/minor strains for Nakazima specimens

A forming failure limit curve (FFLC) is plotted by taking the major and minor strain histories at the center point of each specimen. This is preferred over a forming limit curve (FLC), which takes its end points before the onset of plastic localization, which does not serve as an effective demonstration of the efficacy of a fracture model. Fracture points are selected just before the initiation of the crack. While the trend in fracture behavior for different specimens is captured accurately, the strain values are overstated in comparison to experimental forming limit curves for this material, with some slight divergence in the major/minor strain curves as well. The latter is suspected to occur due to the inherent anisotropy of sheet metals. The study in [96] compares the performance of an anisotropic yield function vs. an isotropic one and concludes that the anisotropic yield function is found to be more successful at reproducing major-minor strain history curves. As for the over-stated fracture strain levels, one possible source of error could be the point at which the material is considered to have failed by preceding studies, where the failure point is chosen relatively earlier than the onset of crack nucleation.

CHAPTER 5

CONCLUSION

This thesis covers the implementation of two fatigue fracture models (crack closure model and representative load model) adopting a diffuse crack methodology to study crack propagation under a fluctuating load. Furthermore, a demonstration is made of the compatibility of phase field modeling of ductile fracture with a phenomenological failure criteria, facilitating a coupled framework while utilizing existing calibrated material parameters.

The crack closure model is based on the work in [32], where the fracture toughness is degraded through an accumulating fatigue damage variable based on fluctuations in the strain energy density. Through an alteration in the fatigue damage accumulation function, crack closure and consequently crack retardation due to overload effects are incorporated. This model is found able to demonstrate crack retardation when an overload is applied. At higher overload levels, greater crack retardation is observed, with the model naturally reproducing the ratio between life gains at higher and lower overload levels. However, this model is found unable to match the high level of life gains observed in experiments when overloads were applied. This may be due to the fact that crack closure is not the sole contributor to crack retardation, with residual stresses at the crack tip also playing a relevant role. Hence future iterations of this model should involve further alterations to the fatigue damage accumulation algorithm to incorporate the influence of crack tip residual stresses.

A study with mixed mode crack propagation is also performed for the crack closure model using a 3-point bending test. It is found that the crack path prediction capabilities of the phase field paradigm have their limitations, particularly in the presence of stop holes. While the results of this thesis seem to suggest that such limitations are

purely computational, it can not be conclusively confirmed.

The representative load model similarly also degrades the fracture toughness and involves a damage accumulation system that involves the application of a representative load, with a temporal accumulation of fatigue damage. In this sense, the boundary conditions are similar to the creep phenomenon. This model incorporates a zone based crack retardation model, slowing down crack growth based on the overload level applied.

This approach is able to successfully reproduce experimental crack life results for overload applications, with the caveat being that a larger number of parameters are required to be calibrated. In this sense, the representative load model may be judged to have performed better than the crack closure model. A relative downside of this model, however, is that the ratio between life gains at various overload levels is not an inherent feature, unlike the crack closure model. Hence several overload cases have to be used for calibration to design an effective retardation model. Furthermore, the models that inspired this one establish a close relationship between the retardation zone size and the retardation co-efficient but that is not featured in the current model. The retardation co-efficient is currently only a function of the overload level. Future work with this model should involve the establishment of such a connection between the zone size and the retardation co-efficient, easing some of the calibration requirement and allowing better performance. Furthermore, this model does not capture the effects of load ratio on the retardation behavior. This influence as well should be incorporated in a future study.

Relative to the crack closure model, the representative load model allows more control over the fatigue response and future works could introduce additional parameters that would allow a more comprehensive simulation of a material's fatigue behavior over a far wider range of loads and load ratios.

The ductile phase field model introduces a plastic component to the crack driving force and is able to incorporate the MMC model into its plastic damage accumulation system, using calibrated MMC parameters to reproduce experimental load-displacement curves for various specimens. Through the addition of a damage threshold, the calibration process of the model is greatly streamlined. The Nakajima test is

simulated to observe the model's efficacy in forming applications and the results are able to reproduce experimental crack patterns as well as an FFLC curve whose trend matches experimentally observed data. This model demonstrates the efficacy of the phase field paradigm for facilitating a non-local, coupled simulation solution for plastic damage models. Future studies involving phase field ductile fracture could explore a variety of alternative ductile damage models, with the model very capable of taking on further complexities with ease.

This thesis has sought to demonstrate the versatility of the phase field paradigm through the imposition of relatively simple numerical controls on the damage accumulation in the context of both fatigue and plasticity.

REFERENCES

[1] T. Belytschko and T. Black, "Elastic crack growth in finite elements with minimal remeshing," *International Journal for Numerical Methods in Engineering*, vol. 45, no. 5, pp. 601–620, 1999.

[2] V. Tvergaard and J. W. Hutchinson, "The influence of plasticity on mixed mode interface toughness," *Journal of the Mechanics and Physics of Solids*, vol. 41, no. 6, pp. 1119–1135, 1993.

[3] X. Zhang, C. Vignes, S. W. Sloan, and D. Sheng, "Numerical evaluation of the phase-field model for brittle fracture with emphasis on the length scale," *Computational Mechanics*, vol. 59, pp. 737–752, 2017.

[4] A. A. Griffith, "The phenomena of rupture and flow in solids," *Philosophical transactions of the royal society of London. Series A, containing papers of a mathematical or physical character*, vol. 221, no. 582-593, pp. 163–198, 1921.

[5] G. A. Francfort and J.-J. Marigo, "Revisiting brittle fracture as an energy minimization problem," *Journal of the Mechanics and Physics of Solids*, vol. 46, no. 8, pp. 1319–1342, 1998.

[6] B. Bourdin, G. A. Francfort, and J.-J. Marigo, "Numerical experiments in revisited brittle fracture," *Journal of the Mechanics and Physics of Solids*, vol. 48, no. 4, pp. 797–826, 2000.

[7] L. Ambrosio and V. M. Tortorelli, "Approximation of functional depending on jumps by elliptic functional via t-convergence," *Communications on Pure and Applied Mathematics*, vol. 43, no. 8, pp. 999–1036, 1990.

[8] D. Mumford and J. Shah, "Boundary detection by minimizing functionals," in *IEEE Conference on Computer Vision and Pattern Recognition*, vol. 17, pp. 137–154, San Francisco, 1985.

[9] C. Miehe, M. Hofacker, and F. Welschinger, "A phase field model for rate-independent crack propagation: Robust algorithmic implementation based on operator splits," *Computer Methods in Applied Mechanics and Engineering*, vol. 199, no. 45-48, pp. 2765–2778, 2010.

[10] G. Molnár, A. Gravouil, R. Seghir, and J. Réthoré, "An open-source abaqus implementation of the phase-field method to study the effect of plasticity on the instantaneous fracture toughness in dynamic crack propagation," *Computer Methods in Applied Mechanics and Engineering*, vol. 365, p. 113004, 2020.

[11] F. Freddi and L. Mingazzi, "Mesh refinement procedures for the phase field approach to brittle fracture," *Computer Methods in Applied Mechanics and Engineering*, vol. 388, p. 114214, 2022.

[12] M. Klinsmann, D. Rosato, M. Kamlah, and R. M. McMeeking, "An assessment of the phase field formulation for crack growth," *Computer Methods in Applied Mechanics and Engineering*, vol. 294, pp. 313–330, 2015.

[13] P. K. Kristensen and E. Martínez-Pañeda, "Phase field fracture modelling using quasi-newton methods and a new adaptive step scheme," *Theoretical and Applied Fracture Mechanics*, vol. 107, p. 102446, 2020.

[14] T. Gerasimov and L. De Lorenzis, "A line search assisted monolithic approach for phase-field computing of brittle fracture," *Computer Methods in Applied Mechanics and Engineering*, vol. 312, pp. 276–303, 2016.

[15] M. J. Borden, C. V. Verhoosel, M. A. Scott, T. J. Hughes, and C. M. Landis, "A phase-field description of dynamic brittle fracture," *Computer Methods in Applied Mechanics and Engineering*, vol. 217, pp. 77–95, 2012.

[16] C. Schreiber, T. Ettrich, C. Kuhn, and R. Müller, "A phase field modeling approach of crack growth in materials with anisotropic fracture toughness," Schloss Dagstuhl-Leibniz-Zentrum für Informatik, 2021.

[17] C. Cui, R. Ma, and E. Martínez-Pañeda, "A phase field formulation for dissolution-driven stress corrosion cracking," *Journal of the Mechanics and Physics of Solids*, vol. 147, p. 104254, 2021.

[18] J. Cheng, X. Tu, and S. Ghosh, "Wavelet-enriched adaptive hierarchical fe model for coupled crystal plasticity-phase field modeling of crack propagation in polycrystalline microstructures," *Computer Methods in Applied Mechanics and Engineering*, vol. 361, p. 112757, 2020.

[19] A. Wöhler, *Über die festigkeitsversuche mit eisen und stahl*. Ernst & Korn, 1870.

[20] H. Mughrabi, "Microstructural fatigue mechanisms: Cyclic slip irreversibility, crack initiation, non-linear elastic damage analysis," *International Journal of Fatigue*, vol. 57, pp. 2–8, 2013.

[21] M. A. Miner, "Cumulative damage in fatigue," *Journal of Applied Mechanics*, 1945.

[22] G. R. Irwin, "Analysis of stresses and strains near the end of a crack traversing a plate," *Journal of Applied Mechanics*, 1957.

[23] P. Paris and F. Erdogan, "A Critical Analysis of Crack Propagation Laws," *Journal of Basic Engineering*, vol. 85, pp. 528–533, 12 1963.

[24] R. G. Forman and S. R. Mettu, "Behavior of surface and corner cracks subjected to tensile and bending loads in Ti-6Al-4V alloy," tech. rep., 1990.

[25] A. Abou Jaoude, "Analytic and linear prognostic model for a vehicle suspension system subject to fatigue," *Systems Science & Control Engineering*, vol. 3, no. 1, pp. 81–98, 2015.

[26] R. O. Ritchie, "Near-threshold fatigue crack propagation in ultra-high strength steel: influence of load ratio and cyclic strength," 1977.

[27] H. Pathak, A. Singh, and I. V. Singh, "Fatigue crack growth simulations of 3-D problems using XFEM," *International Journal of Mechanical Sciences*, vol. 76, pp. 112–131, 2013.

[28] H. Dirik and T. Yalçinkaya, "Fatigue crack growth under variable amplitude loading through XFEM," *Procedia Structural Integrity*, vol. 2, pp. 3073–3080, 2016.

[29] H. Dirik and T. Yalçinkaya, "Crack path and life prediction under mixed mode cyclic variable amplitude loading through XFEM," *International Journal of Fatigue*, vol. 114, pp. 34–50, 2018.

[30] G. Zhang, Q. Le, A. Loghin, A. Subramaniyan, and F. Bobaru, "Validation of a peridynamic model for fatigue cracking," *Engineering Fracture Mechanics*, vol. 162, pp. 76–94, 2016.

[31] R. Alessi, S. Vidoli, and L. De Lorenzis, "A phenomenological approach to fatigue with a variational phase-field model: The one-dimensional case," *Engineering fracture mechanics*, vol. 190, pp. 53–73, 2018.

[32] P. Carrara, M. Ambati, R. Alessi, and L. De Lorenzis, "A framework to model the fatigue behavior of brittle materials based on a variational phase-field approach," *Computer Methods in Applied Mechanics and Engineering*, vol. 361, p. 112731, 2020.

[33] W. Ai, B. Wu, and E. Martínez-Pañeda, "A coupled phase field formulation for modelling fatigue cracking in lithium-ion battery electrode particles," *Journal of Power Sources*, vol. 544, p. 231805, 2022.

[34] M. Simoes and E. Martínez-Pañeda, "Phase field modelling of fracture and fatigue in shape memory alloys," *Computer Methods in Applied Mechanics and Engineering*, vol. 373, p. 113504, 2021.

[35] Y.-S. Lo, M. J. Borden, K. Ravi-Chandar, and C. M. Landis, "A phase-field model for fatigue crack growth," *Journal of the Mechanics and Physics of Solids*, vol. 132, p. 103684, 2019.

[36] P. J. Loew, L. H. Poh, B. Peters, and L. A. Beex, "Accelerating fatigue simulations of a phase-field damage model for rubber," *Computer Methods in Applied Mechanics and Engineering*, vol. 370, p. 113247, 2020.

[37] C. Schreiber, C. Kuhn, R. Müller, and T. Zohdi, "A phase field modeling approach of cyclic fatigue crack growth," *International Journal of Fracture*, vol. 225, pp. 89–100, 2020.

[38] M. Seiler, T. Linse, P. Hantschke, and M. Kästner, "An efficient phase-field model for fatigue fracture in ductile materials," *Engineering Fracture Mechanics*, vol. 224, p. 106807, 2020.

[39] K. Seleš, F. Aldakheel, Z. Tonković, J. Sorić, and P. Wriggers, "A general phase-field model for fatigue failure in brittle and ductile solids," *Computational Mechanics*, vol. 67, no. 5, pp. 1431–1452, 2021.

[40] R. Pippan and A. Hohenwarter, "Fatigue crack closure: a review of the physical phenomena," *Fatigue & Fracture of Engineering Materials & structures*, vol. 40, no. 4, pp. 471–495, 2017.

[41] E. Wolf, "Fatigue crack closure under cyclic tension," *Engineering Fracture Mechanics*, vol. 2, no. 1, pp. 37–45, 1970.

[42] J. Schijve, "Fatigue damage accumulation and incompatible crack front orientation," *Engineering Fracture Mechanics*, vol. 6, no. 2, pp. 245–252, 1974.

[43] J. Schijve, "The accumulation of fatigue damage in aircraft materials and structures," tech. rep., Advisory Group for Aerospace Research and Development Neuilly-sur-Seine (France), 1972.

[44] G. Wheatley, X. Hu, and Y. Estrin, "Effects of a single tensile overload on fatigue crack growth in a 316l steel," *Fatigue and Fracture of Engineering Materials and Structures*, vol. 22, pp. 1041–1051, 1999.

[45] S. Suresh, "Micromechanisms of fatigue crack growth retardation following overloads," *Engineering Fracture Mechanics*, vol. 18, no. 3, pp. 577–593, 1983.

[46] J. A. Correia, A. M. De Jesus, P. M. Moreira, and P. J. Tavares, "Crack closure effects on fatigue crack propagation rates: application of a proposed theoretical model," *Advances in Materials Science and Engineering*, vol. 2016, 2016.

[47] J. Newman Jr, "A crack opening stress equation for fatigue crack growth," *International Journal of fracture*, vol. 24, 1984.

[48] O. E. Wheeler, "Spectrum Loading and Crack Growth," *Journal of Basic Engineering*, vol. 94, pp. 181–186, 03 1972.

[49] J. Willenborg, R. Engle, and H. Wood, "A crack growth retardation model using an effective stress concept," tech. rep., Air Force Flight Dynamics Lab Wright-Patterson Afb Oh, 1971.

[50] P. Noell, J. Carroll, B. L. Boyce, K. M. Hattar, and B. Clark, "Void initiation during ductile rupture of pure metals.," tech. rep., Sandia National Lab.(SNL-NM), Albuquerque, NM (United States), 2018.

[51] J. Gurland and J. Plateau, "The mechanism of ductile rupture of metals containing inclusions," tech. rep., Brown Univ., Providence; Institut de Recherches de la Siderugie, St.-Germain . . . , 1963.

[52] C. Lui, "The fracture behavior of spheroidized carbon steels," *Transactions of American Society for Metals*, vol. 61, pp. 156–167, 1968.

[53] J. Besson, "Continuum models of ductile fracture: a review," *International Journal of Damage Mechanics*, vol. 19, no. 1, pp. 3–52, 2010.

[54] J. Besson, D. Steglich, and W. Brocks, "Modeling of crack growth in round bars and plane strain specimens," *International Journal of Solids and Structures*, vol. 38, no. 46-47, pp. 8259–8284, 2001.

[55] A. E. O. Tuhami, S. Feld-Payet, S. Quilici, N. Osipov, and J. Besson, "A two characteristic length nonlocal gtn model: Application to cup–cone and slant fracture," *Mechanics of Materials*, vol. 171, p. 104350, 2022.

[56] Z. P. Bazant, "Mechanics of distributed cracking," *Appl. Mech. Rev*, vol. 39, no. 5, pp. 675–705, 1986.

[57] Y. Bao and T. Wierzbicki, "On fracture locus in the equivalent strain and stress triaxiality space," *International journal of mechanical sciences*, vol. 46, no. 1, pp. 81–98, 2004.

[58] Y. Bai and T. Wierzbicki, "Application of extended Mohr–Coulomb criterion to ductile fracture," *International Journal of Fracture*, vol. 161, no. 1, pp. 1–20, 2010.

[59] H. Vural, C. Erdoğan, T. O. Fenercioğlu, and T. Yalçinkaya, "Ductile failure prediction during the flow forming process," *Procedia Structural Integrity*, vol. 35, pp. 25–33, 2022.

[60] C. Erdoğan, H. Vural, T. O. Fenercioğlu, and T. Yalçinkaya, "Effect of process parameters on the ductile failure behavior of flow forming process," *Procedia Structural Integrity*, vol. 42, pp. 1643–1650, 2022.

[61] G. R. Johnson and W. H. Cook, "Fracture characteristics of three metals subjected to various strains, strain rates, temperatures and pressures," *Engineering fracture mechanics*, vol. 21, no. 1, pp. 31–48, 1985.

[62] M. J. Borden, T. J. Hughes, C. M. Landis, A. Anvari, and I. J. Lee, "A phase-field formulation for fracture in ductile materials: Finite deformation balance law derivation, plastic degradation, and stress triaxiality effects," *Computer Methods in Applied Mechanics and Engineering*, vol. 312, pp. 130–166, 2016.

[63] C. Li, J. Fang, C. Wu, G. Sun, G. Steven, and Q. Li, "Phase field fracture in elasto-plastic solids: Incorporating phenomenological failure criteria for ductile materials," *Computer Methods in Applied Mechanics and Engineering*, vol. 391, p. 114580, 2022.

[64] S. A. Vajari, M. Neuner, P. K. Arunachala, A. Ziccarelli, G. Deierlein, and C. Linder, "A thermodynamically consistent finite strain phase field approach to ductile fracture considering multi-axial stress states," *Computer Methods in Applied Mechanics and Engineering*, vol. 400, p. 115467, 2022.

[65] R. Alessi, J.-J. Marigo, and S. Vidoli, "Gradient damage models coupled with plasticity and nucleation of cohesive cracks," *Archive for Rational Mechanics and Analysis*, vol. 214, no. 2, pp. 575–615, 2014.

[66] K. Pham, H. Amor, J.-J. Marigo, and C. Maurini, "Gradient damage models and their use to approximate brittle fracture," *International Journal of Damage Mechanics*, vol. 20, no. 4, pp. 618–652, 2011.

[67] G. Molnár and A. Gravouil, "2D and 3D abaqus implementation of a robust staggered phase-field solution for modeling brittle fracture," *Finite Elements in Analysis and Design*, vol. 130, pp. 27–38, 2017.

[68] K. Pham, J.-J. Marigo, and C. Maurini, "The issues of the uniqueness and the stability of the homogeneous response in uniaxial tests with gradient damage models," *Journal of the Mechanics and Physics of Solids*, vol. 59, no. 6, pp. 1163–1190, 2011.

[69] M. J. Borden, T. J. Hughes, C. M. Landis, and C. V. Verhoosel, "A higher-order phase-field model for brittle fracture: Formulation and analysis within the isogeometric analysis framework," *Computer Methods in Applied Mechanics and Engineering*, vol. 273, pp. 100–118, 2014.

[70] M. E. Gurtin, "Generalized Ginzburg-Landau and Cahn-Hilliard equations based on a microforce balance," *Physica D: Nonlinear Phenomena*, vol. 92, no. 3-4, pp. 178–192, 1996.

[71] L. Svolos, J. N. Plohr, G. Manzini, and H. M. Mourad, "On the convexity of phase-field fracture formulations: Analytical study and comparison of various degradation functions," *International Journal of Non-Linear Mechanics*, p. 104359, 2023.

[72] H. Amor, J.-J. Marigo, and C. Maurini, "Regularized formulation of the variational brittle fracture with unilateral contact: Numerical experiments," *Journal of the Mechanics and Physics of Solids*, vol. 57, no. 8, pp. 1209–1229, 2009.

[73] Y. Navidtehrani, C. Betegón, and E. Martínez-Pañeda, "A unified abaqus implementation of the phase field fracture method using only a user material subroutine," *Materials*, vol. 14, no. 8, p. 1913, 2021.

[74] P. K. Kristensen, C. F. Niordson, and E. Martínez-Pañeda, "An assessment of phase field fracture: crack initiation and growth," *Philosophical Transactions of the Royal Society A*, vol. 379, no. 2203, p. 20210021, 2021.

[75] Z. Liu, J. Reinoso, and M. Paggi, "Phase field modeling of brittle fracture in large-deformation solid shells with the efficient quasi-Newton solution and global–local approach," *Computer Methods in Applied Mechanics and Engineering*, vol. 399, p. 115410, 2022.

[76] Y.-c. Lu, F.-p. Yang, and T. Chen, "Effect of single overload on fatigue crack

growth in QSTE340TM steel and retardation model modification," *Engineering Fracture Mechanics*, vol. 212, pp. 81–94, 2019.

[77] M. Mehrzadi and F. Taheri, "A material sensitive modified wheeler model for predicting the retardation in fatigue response of AM60B due to an overload," *International Journal of Fatigue*, vol. 55, pp. 220–229, 2013.

[78] A. R. Ingraffea and M. Grigoriu, "Probabilistic fracture mechanics: A validation of predictive capability," *Department of Structural Engineering. Technical report, Cornell University*, 1990.

[79] W. Elber, "The significance of fatigue crack closure," 1971.

[80] S. Waseem, İzzet Erkin Ünsal, and T. Yalçinkaya, "Phase field modelling of fatigue crack growth at constant and variable amplitude loading," *Procedia Structural Integrity*, vol. 42, pp. 1692–1699, 2022. 23 European Conference on Fracture.

[81] J. Schijve, *Stress Intensity Factors of Cracks*. 01 2004.

[82] B. Budiansky and J. Hutchinson, "Analysis of closure in fatigue crack growth," *Journal of Applied Mechanics*, vol. 45, no. 2, pp. 267–276, 1978.

[83] R. E. Jones, "Fatigue crack growth retardation after single-cycle peak overload in Ti-6Al-4V titanium alloy," *Engineering Fracture Mechanics*, vol. 5, no. 3, pp. 585–604, 1973.

[84] J.-Y. Wu and V. P. Nguyen, "A length scale insensitive phase-field damage model for brittle fracture," *Journal of the Mechanics and Physics of Solids*, vol. 119, pp. 20–42, 2018.

[85] A. Golahmar, C. F. Niordson, and E. Martínez-Pañeda, "A phase field model for high-cycle fatigue: Total-life analysis," *International Journal of Fatigue*, vol. 170, p. 107558, 2023.

[86] F. P. Duda, A. Ciarbonetti, P. J. Sánchez, and A. E. Huespe, "A phase-field/gradient damage model for brittle fracture in elastic–plastic solids," *International Journal of Plasticity*, vol. 65, pp. 269–296, 2015.

[87] M. Ambati, T. Gerasimov, and L. De Lorenzis, "Phase-field modeling of ductile fracture," *Computational Mechanics*, vol. 55, no. 5, pp. 1017–1040, 2015.

[88] B. Yin and M. Kaliske, "A ductile phase-field model based on degrading the fracture toughness: Theory and implementation at small strain," *Computer Methods in Applied Mechanics and Engineering*, vol. 366, p. 113068, 2020.

[89] M. Dittmann, F. Aldakheel, J. Schulte, F. Schmidt, M. Krüger, P. Wriggers, and C. Hesch, "Phase-field modeling of porous-ductile fracture in non-linear thermo-elasto-plastic solids," *Computer Methods in Applied Mechanics and Engineering*, vol. 361, p. 112730, 2020.

[90] D. Proserpio, M. Ambati, L. De Lorenzis, and J. Kiendl, "Phase-field simulation of ductile fracture in shell structures," *Computer Methods in Applied Mechanics and Engineering*, vol. 385, p. 114019, 2021.

[91] H. Ulmer, M. Hofacker, and C. Miehe, "Phase field modeling of brittle and ductile fracture," *Pamm*, vol. 13, no. 1, pp. 533–536, 2013.

[92] H. Granum, D. Morin, T. Børvik, and O. S. Hopperstad, "Calibration of the modified Mohr-Coulomb fracture model by use of localization analyses for three tempers of an AA6016 aluminium alloy," *International Journal of Mechanical Sciences*, vol. 192, p. 106122, 2021.

[93] C. Erdogan, H. Vural, A. Karakaş, T. O. Fenercioğlu, and T. Yalçinkaya, "Ductile failure of inconel 718 during flow forming process and its numerical investigation," *Engineering Failure Analysis*, vol. 152, p. 107424, 2023.

[94] M. Cockcroft and D. Lathan, *Ductility and the Workability of Metals*. 1968.

[95] R. Amaral, A. D. Santos, C. de Sá José, and S. Miranda, "Formability prediction for AHSS materials using damage models," in *Journal of Physics: Conference Series*, vol. 843, p. 012018, IOP Publishing, 2017.

[96] M. B. Gorji and D. Mohr, "Predicting shear fracture of aluminum 6016-T4 during deep drawing: Combining Yld-2000 plasticity with Hosford–Coulomb fracture model," *International Journal of Mechanical Sciences*, vol. 137, pp. 105–120, 2018.